Field-controlled flow and shape of a magnetorheological fluid annulus

Írio M. Coutinho [*] and José A. Miranda [†]

Departamento de Física, Universidade Federal de Pernambuco, 50670-901 Recife, Pernambuco, Brazil

We investigate the behavior of a magnetorheological (MR) fluid annulus, bounded by a nonmagnetic fluid and confined in a Hele-Shaw cell, under the simultaneous effect of in-plane, external radial and azimuthal magnetic fields. A second-order mode-coupling theory is used to study the early nonlinear stage of the pattern-forming dynamics. We examine changes in the morphology of the MR fluid annular structure as a function of its magnetic-field-tunable rheological properties, as well as the combined magnetic field's intensities, and thickness of the ring. Our weakly nonlinear perturbative results show that, depending on the system control parameters, the MR fluid annulus adopts various stationary shapes. These equilibrium annular structures present slightly bent, asymmetric fingered protrusions which may emerge on the inner, outer, or even on both boundaries of the magnetic fluid ring. On top of these morphological changes, we find that the resulting permanent shape patterns rotate with a well defined angular velocity. We focus on analyzing how the overall shape of the fingered patterns, in particular their sharpness and asymmetric form, as well as the number of resulting fingers are impacted by the magnetic-field-dependent yield stress of the MR fluid annulus. The influence of the magnetically controlled rheological properties of the MR fluid on the angular velocity of the rotating annulus is also scrutinized.

I. INTRODUCTION

Smart fluid materials such as ferrofluids and magnetorheological (MR) fluids have the distinguishing feature of associating magnetic adjustable properties of solids, with usual fluidity behaviors of liquids. Ferrofluids are stable colloidal suspensions of monodomain, nanometer-size magnetic particles suspended in a nonmagnetic solvent. In ferrofluids, the tiny magnetic particles show no tendency to form chains, and consequently most ferrofluids are Newtonian fluids [1–3]. Differently, MR fluids are suspensions of multidomain, micrometer-size magnetic particles in a nonmagnetic carrier fluid. In MR fluids, the magnetic particles tend to aggregate into chainlike structures, inducing significant changes in their physical properties. A particularly interesting facet of MR fluids is the abrupt modification in their viscoelastic attributes upon the action of an external magnetic field, allowing them to change from a liquid to a solidlike state very quickly. As a result, unlike ferrofluids, MR fluids are markedly non-Newtonian [4–6], being characterized by a magnetic-field-dependent yield stress behavior [7,8].

Because of their special physical properties and ability to be manipulated and shaped by external magnetic fields, these magnetic fluids have attracted increasing interest in several areas ranging from physics, chemistry, engineering, and robotics, through biology and medicine [9–18]. In particular, the easy and versatile handling of the ferrofluids' flow and shape via magnetic means has motivated researchers to use them as multitask, magnetically activated agents in microfluidics, micromixing, and in the dynamics and manipulation of soft robots [19–25]. In these studies, investigators utilized magnetic fields to actuate and control ferrofluid droplets as shape-programmable magnetic fluid objects, which can navigate through very narrow channels, carrying liquid samples and fragile objects, or mixing chemicals in spatially confined environments. A particularly interesting ability of these ferrofluid manageable tools has been studied in Refs. [24,25] where ferrofluid droplets are configured into a ring shape, and used to collect, transport, and release multiple delicate items quite effectively. As mentioned in Refs. [24,25], the magnetic controllability of ferrofluid annular ring structures potentially permits the development of innovative functionalities in lab-on-a-chip, microfluidics, bioengineering, and biomedical applications.

Despite the considerably large number of recent studies on ferrofluid soft robot systems and related topics (see, for instance, Refs. [19–25] and references therein), equivalent investigations utilizing MR fluid-based robots have not received much attention in the literature. One noteworthy exception is the very recent work by Sun *et al.* [26,27] who considered magnetic soft-bodied robots made of a MR fluid (the so-called magnetic slime robot). As discussed in Ref. [26], MR fluids present some advantages over ferrofluids when one desires navigation through narrow channels, and highly spatially restricted environments. For instance, most ferrofluid-based droplet robots require relatively demanding operating conditions, such as hydrophilic surfaces surrounded by water-based solutions, to keep their original shape, as well as to prevent them from adhering to the substrate. Conversely, as demonstrated in Ref. [26], MR fluid soft robots can easily move on various types of substrates, including hydrogel, glass, metallic, and plastic surfaces.

---

[*]irio.menezes@ufpe.br
[†]jose.mirandant@ufpe.br

Another advantage of using MR fluids noted in Ref. [26] is connected to the response of magnetic fluid droplets to applied magnetic fields. For example, although the deformability of ferrofluid droplet robots is the best under low magnetic field magnitudes, as the applied magnetic field strength increases, the ferrofluid droplet shape becomes increasingly unstable, and it is difficult to keep the drop intact. On the other hand, due to their non-Newtonian nature, MR fluid droplets exhibit a tunable stiffness under applied magnetic fields. Therefore, MR fluid-based droplet robots are capable of entering and moving through confined spaces in a controllable way while maintaining their integrity, even at high magnetic field strengths. In other words, even at large applied field conditions, the MR fluid droplet robots can deform without breaking up into smaller secondary droplets.

The magnetic-field-controlled deformation and stiffness of MR fluid droplets give them a considerable advantage over their ferrofluid counterparts. This is particularly valid for the useful ring-shaped robots [24,25] which can keep their annular conformation intact while they move, maintaining their cargo contents inside the ring and not letting them escape to the external environment. The broadly applicable working environment of the MR fluid-based robots under a wide range of magnetic field strengths as well as their largely deformable, reconfigurable, and magnetically tuned viscoelastic properties make them promising for future applications in many fields, including controlled drug delivery [28], microfluidics [29], and micromixing [30]. Therefore, these propitious applications are not restricted to ferrofluids, and can even become more effective if MR fluids are utilized [26].

Since ferrofluids and MR fluids can move through constrained, effectively two-dimensional channels, exhibiting various magnetically regulated, complex shape-morphing behaviors, they are natural candidates for the study of the dynamics of pattern-forming structures in the confined geometry of Hele-Shaw cells (i.e., between two closely spaced parallel glass plates) [31,32]. As a matter of fact, the Hele-Shaw cell apparatus, assisted by proper magnetic field arrangements, can be used as an ideal laboratory system, and as a testing ground for a number of possible applications involving magnetic fluid-based soft robots. However, most existing studies [19–26] consider ferrofluid and MR fluid droplets moving through relatively complex terrains such as intricate tubes, complicated mazes, and uneven substrates. Furthermore, the majority of these investigations examine situations in which the controlling magnetic fields are significantly convoluted as the ones produced by electromagnet arrays, or permanent magnets of various shapes, either in translational or rotational movements.

The consideration of the motion of ferrofluid or MR fluid droplets in the simpler geometry of a Hele-Shaw cell, and under the influence of substantially less complicated magnetic field configurations, would help one to model and try to better understand the fundamental physical processes leading the appealing behaviors of the magnetic fluid droplets reported in Refs. [19–26]. An example of such a simplified theoretical study has been recently performed in Ref. [33], where the authors, inspired by Refs. [24,25], analyzed the pattern-forming dynamics of a *ferrofluid annulus* surrounded by nonmagnetic fluids, confined in a Hele-Shaw cell, and

subjected to an in-plane, crossed magnetic field arrangement. External magnetic field effects are induced by the concurrent action of both radial and azimuthal applied magnetic fields. This particular magnetic field setup was proposed in the literature not long ago [34], and is fairly simple: the azimuthal magnetic field is produced by a current-carrying wire which is normal to the Hele-Shaw cell plates and passes through its center [35,36], while the radial field is produced by a pair of identical Helmholtz coils whose electric currents are equal, and flow in opposite directions [37,38]. The utilization of these crossed magnetic fields adds ample versatility into the system, allowing separate bidirectional magnetic control of the inner and outer interfaces of the magnetic fluid annular ring. In this way, both inhibition and promotion of interfacial instabilities are possible by properly tuning the strength of azimuthal and radial fields. In addition, as demonstrated in Refs. [33,34,39], the crossed magnetic fields induce rotation of the magnetic fluid sample, which achieves a stable profile shape, spinning with a prescribed, magnetically controllable angular velocity.

We note that there are well justified reasons to consider magnetic fluids of annular ring shape under crossed magnetic fields. First, as commented earlier in this work, it has been shown in Refs. [24–26] that ring-shaped magnetic fluid droplets driven by permanent magnets can be useful controlling tools in the sense that they can be used to trap, transport, and deliver multiple delicate objects efficiently in confined spaces. As previously observed, this opens up potential functionalities in many technological and medical applications. Therefore, it is of considerable practical interest to investigate the magnetic manipulation of such smart-fluid annular structures in Hele-Shaw cells, under the simpler crossed magnetic field setup which is more amenable to theoretical analysis. On top of this, recall that the crossed magnetic fields can make the magnetic liquid ring rotate, so it could also be used to promote efficient fluid mixing at low Reynolds numbers in narrow channels, something of great current interest [30]. On a more academic side, the magnetic fluid annulus setup is of relevance due to its own doubly connected character which comprises the nontrivial interaction between two separate interfaces (the inner and outer boundaries of the annular ring structure). This allows one to seek still unexplored pattern-forming behaviors, and dynamical responses not exhibited in simply connected situations in which only a single interface separates the magnetic and nonmagnetic fluids.

The theoretical study performed in Ref. [33] has shown that by adjusting the radial and azimuthal components of the applied crossed magnetic field, and by changing the thickness of the ferrofluid annulus, one finds a number of different steady state annular-shaped patterns, typically presenting a polygonal-like appearance. These ring-shaped structures have skewed fingered protuberances having relatively sharp peaks that may arise on the inner, outer, or even on both boundaries of the ferrofluid ring. Moreover, it has been found that of on top of these magnetically tuned morphological changes, the crossed magnetic fields can be utilized to regulate both the magnitude and direction of the annulus rotational motion.

It should be pointed out that an investigation similar to the one performed in Ref. [33], but considering a *MR fluid annulus*, still needs to be performed. Taking this fact into
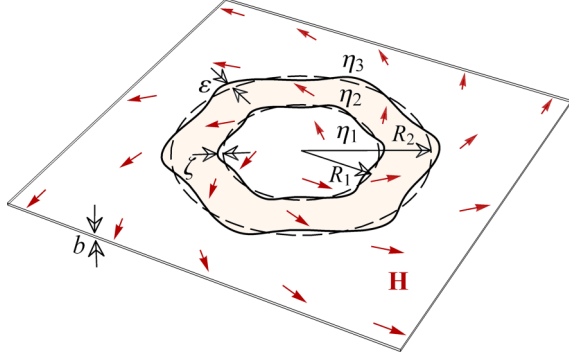
FIG. 1. Schematic of the MR fluid annulus confined flow problem subjected to a combined (radial plus azimuthal) magnetic field **H** [Eq. (3)]. Initially, the MR fluid annular structure of viscosity η_2 has circular boundaries, of radii R_1 and R_2 (dashed circles). The inner and outer fluids are nonmagnetic and Newtonian, having viscosities η_1 and η_3, respectively. The magnetic field **H** may distort the inner and outer perimeters of the MR fluid annulus (solid curves). The perturbed inner interface of the MR fluid ring is described by $\mathcal{R}_1(\theta, t) = R_1 + \zeta(\theta, t)$, where $\zeta = \zeta(\theta, t)$ is a time-varying interfacial perturbation amplitude, and θ is the azimuthal angle. Similarly, the perturbed outer interface of the annulus is expressed as $\mathcal{R}_2(\theta, t) = R_2 + \varepsilon(\theta, t)$.

consideration, and motivated by the compelling findings reported by Sun and collaborators [26,27] who studied magnetically reconfigurable MR fluid-based soft robots, we anticipate that the problem of magnetic-field-manipulated MR fluid annular ring structures in a simple spatially confined geometry is of interest, and worth investigating. Therefore, in this work we examine the flow dynamics and interfacial pattern formation phenomena that arise when a MR fluid ring bounded by a nonmagnetic fluid is subjected to crossed magnetic fields in a Hele-Shaw cell.

By using a modified Darcy's law approach which incorporates a magnetic-field-dependent yield stress behavior of the MR fluid annulus, we employ a second-order mode-coupling theory to investigate the initial nonlinear regime of the system, and to obtain perturbative solutions for the shape of the confined MR fluid annular patterns. We identify the formation of permanent profile, stationary state, spinning annular shapes, showing slightly curved fingers. We focus on examining how the magnetic-field-dependent yield stress of the non-Newtonian MR fluid annulus affects the overall morphology and stability of the ring-shaped patterns, and the number of resulting fingered structures. We also analyze how the magnetic-field-dependent yield stress impacts the angular velocity of the rotating MR fluid annulus, as well as the sharpness and asymmetric form of the internal and external interfaces of the ring. All this is done for various thicknesses of the MR fluid ring, and also for different relative magnitudes of the radial and azimuthal magnetic field components.

II. PROBLEM FORMULATION AND BASIC EQUATIONS

The geometry of the physical system is shown schematically in Fig. 1. A Hele-Shaw cell of gap thickness b contains a MR fluid annular structure of viscosity η_2 under the in-

fluence of in-plane, crossed magnetic fields. The MR fluid annulus is surrounded by two nonmagnetic Newtonian fluids of viscosities η_1 and η_3. All three fluids are immiscible and incompressible, with the surface tension between the MR fluid and the inner (outer) nonmagnetic fluid denoted by σ_{12} (σ_{23}). Initially, due to surface tension forces, the MR fluid annular ring has circular boundaries of radii R_1 and R_2. Nevertheless, the action of the applied magnetic fields may deform the inner and outer borders of the MR fluid annulus, delimiting it by the perturbed, time-dependent interfaces $\mathcal{R}_1 = \mathcal{R}_1(\theta, t)$ and $\mathcal{R}_2 = \mathcal{R}_2(\theta, t)$, where θ is the azimuthal angle. In this section, our main goal is to describe the time evolution of the inner and outer interfaces of the deformed MR fluid annulus at early nonlinear stages of the dynamics.

Under the spatially constrained conditions of Hele-Shaw flows in the presence of external applied magnetic fields, and using the Bingham model for yield-stress fluids [40], the quasi-two-dimensional dynamics of the MR fluid interfaces is described by a gap-averaged, modified Darcy's law [7,8,39,41–46]

$$\mathbf{v}_j|_{r=\mathcal{R}_1} = -\frac{b^2}{12\eta_j}\left\{\boldsymbol{\nabla}\Pi_j - \frac{3\sigma_y(H)}{b}\hat{\mathbf{e}}_r\right\}, \qquad (1)$$

for the inner interface (with $j = 1, 2$), and

$$\mathbf{v}_j|_{r=\mathcal{R}_2} = -\frac{b^2}{12\eta_j}\left\{\boldsymbol{\nabla}\Pi_j + \frac{3\sigma_y(H)}{b}\hat{\mathbf{e}}_r\right\}, \qquad (2)$$

for the outer interface (with $j = 2, 3$), where the labels $j = 1$, 2, and 3 refer to the inner, intermediate (annulus), and outer fluids, respectively. In Eqs. (1) and (2), Π_j is a generalized pressure, $\sigma_y(H)$ is a magnetic-field-dependent yield stress, $H = |\mathbf{H}|$ denotes the combined magnetic field intensity, and $\hat{\mathbf{e}}_r$ represents a unit vector in the radial direction. The derivations of Eqs. (1) and (2) assume the regime where magnetic and viscous forces prevail over the stabilizing role of the yield stress. In addition, based on the fact that both radial and azimuthal magnetic fields produce magnetic body forces directed radially [1,35,37], it is also assumed that the prevalent yielding occurs along the radial direction.

The applied magnetic field is given by [34,39]

$$\mathbf{H} = H_0 r\,\hat{\mathbf{e}}_r + \frac{I}{2\pi r}\,\hat{\mathbf{e}}_\theta, \qquad (3)$$

where the first (second) term on the right-hand side of Eq. (3) expresses the applied radial (azimuthal) field, H_0 is a constant, I is a time-independent electric current, and $\hat{\mathbf{e}}_\theta$ represents the unit vector along the azimuthal direction. This combined applied field relates to the shear yield stress by [4–8]

$$\sigma_y(H) = \sigma_{y0} + \alpha H^2, \qquad (4)$$

where σ_{y0} is a small yield stress present in the absence of magnetic field, and α is a constant that depends on the material properties of the MR fluid, being proportional to the particle volume fraction [6].

In Eqs. (1) and (2), the gap-averaged generalized pressure is defined as [42–44]

$$\Pi_j = \frac{1}{b}\int_{-b/2}^{+b/2}[P_j - \Psi]dz, \qquad (5)$$

where P_j is the three-dimensional fluid pressure, and

$$\Psi = \frac{\mu_0 \chi H^2}{2} \tag{6}$$

represents a scalar potential accounting for the magnetic body force [1,2], where μ_0 is the magnetic permeability of free space, and χ the magnetic susceptibility. A magnetization **M** linear with the applied field [1,2,47] is assumed, such that $\mathbf{M} = \chi \mathbf{H}$. Note that for the nonmagnetic fluids surrounding the MR fluid annulus we have that $\chi = \Psi = 0$.

As the field-dependent yield-stress terms [second terms in curly brackets of Eqs. (1) and (2)] can be expressed as gradients of some scalar functions, and since the velocity fields are irrotational in the bulk, we can conveniently express the velocities in terms of velocity potentials, such that $\mathbf{v}_j = -\nabla\phi_j$. Moreover, using this fact and the incompressibility condition $\nabla \cdot \mathbf{v_j} = 0$, one concludes that the velocity potentials obey Laplace's equation $\nabla^2 \phi_j = 0$. Therefore, to fully describe the problem at the fluid-fluid interfaces, two fundamental boundary conditions for each interface of the MR fluid annulus are needed. The first pair comes from the discontinuity of the pressure field across the interfaces, given by modified Young-Laplace equations [1,2]

$$(p_1 - p_2)|_{r=\mathcal{R}_1} = \left[\sigma_{12}\kappa_{12} + \tfrac{1}{2}\mu_0(\mathbf{M}\cdot\hat{\mathbf{n}})^2 \right]\big|_{r=\mathcal{R}_1} \tag{7}$$

and

$$(p_2 - p_3)|_{r=\mathcal{R}_2} = \left[\sigma_{23}\kappa_{23} - \tfrac{1}{2}\mu_0(\mathbf{M}\cdot\hat{\mathbf{n}})^2 \right]\big|_{r=\mathcal{R}_2}, \tag{8}$$

where κ_{12} and κ_{23} are the interfacial curvatures of the inner and outer interfaces in the plane of the Hele-Shaw cell, respectively. The second terms on the right-hand sides of Eqs. (7) and (8) express magnetic traction effects [1,2] arising from the influence of the normal component of the MR fluid magnetization at the inner and outer interfaces of the annulus, where the unit normal vector at each interface is represented by $\hat{\mathbf{n}}|_{r=\mathcal{R}_{1,2}}$. We point out that the contribution of such magnetic normal stresses is an intrinsically nonlinear concern, and is not required in the purely linear stability analysis of the problem. In fact, this particular magnetic normal traction term has a key role in determining the shape of the emergent interfacial patterns in a magnetic fluid annulus [33,34,39].

The second pair of boundary conditions arises from the continuity of the normal components of the flow velocities at the inner and outer boundaries of the MR fluid annulus, expressed by the so-called kinematic boundary conditions [31,32]

$$\frac{\partial \mathcal{R}_1}{\partial t} = \left(\frac{1}{r^2} \frac{\partial \mathcal{R}_1}{\partial \theta} \frac{\partial \phi_j}{\partial \theta} \right)\bigg|_{r=\mathcal{R}_1} - \left(\frac{\partial \phi_j}{\partial r} \right)\bigg|_{r=\mathcal{R}_1} \tag{9}$$

for the inner interface (with $j = 1, 2$), and

$$\frac{\partial \mathcal{R}_2}{\partial t} = \left(\frac{1}{r^2} \frac{\partial \mathcal{R}_2}{\partial \theta} \frac{\partial \phi_j}{\partial \theta} \right)\bigg|_{r=\mathcal{R}_2} - \left(\frac{\partial \phi_j}{\partial r} \right)\bigg|_{r=\mathcal{R}_2} \tag{10}$$

for the outer interface (with $j = 2, 3$).

With the Darcy's law expressions (1) and (2), and the related boundary conditions given by Eqs. (7)–(10), we have all elements needed to develop a perturbative, second-order mode-coupling theory for our problem [39,48]. In the remainder of this work, for the sake of simplicity, we set the

two nonmagnetic fluids to be the same, yielding $\eta_3 = \eta_1$ and $\sigma_{12} = \sigma_{23} = \sigma$, where here σ denotes the surface tension between the MR fluid and the nonmagnetic fluid. Additionally, we consider that the MR fluid is much more viscous than the nonmagnetic fluid ($\eta_2 \gg \eta_1$). In this context, recall that the inner fluid-fluid interface is given by $\mathcal{R}_1(\theta, t) = R_1 + \zeta(\theta, t)$, where now the interfacial perturbation is written in the form of a Fourier series

$$\zeta(\theta, t) = \sum_{n=-\infty}^{+\infty} \zeta_n(t) \, e^{in\theta}, \tag{11}$$

where $\zeta_n(t)$ denotes the complex Fourier amplitudes, with integer wave numbers n. Analogously, for the outer interface of the MR fluid annular ring, we write $\mathcal{R}_2(\theta, t) = R_2 + \epsilon(\theta, t)$, with

$$\varepsilon(\theta, t) = \sum_{n=-\infty}^{+\infty} \varepsilon_n(t) \, e^{in\theta}. \tag{12}$$

Mass conservation dictates that the zeroth mode is cast in terms of the other modes as $\zeta_0 = -(1/2R_1)\sum_{n=1}^{\infty} [|\zeta_n(t)|^2 + |\zeta_{-n}(t)|^2]$ [33,48]. Likewise, we have $\varepsilon_0 = -(1/2R_2)\sum_{n=1}^{\infty} [|\varepsilon_n(t)|^2 + |\varepsilon_{-n}(t)|^2]$.

Instead of being limited to a simple linear stability analysis of the problem, we employ a second-order mode-coupling approach which allows us to explore and gain insight into key aspects of the MR fluid annulus's morphology at the onset of nonlinear effects. Since we are interested in the early nonlinear behavior of the system, we want to obtain a set of mode-coupling nonlinear differential equations which describe the time evolution of the perturbation amplitudes $\zeta_n(t)$ and $\varepsilon_n(t)$, accurate to second order. To accomplish this, we follow steps similar to those performed in previous weakly nonlinear studies in Hele-Shaw flows [48,49]: First, we Fourier expand the velocity potentials, and use the kinematic conditions [Eqs. (9) and (10)] to express the Fourier coefficients of velocity potentials in terms of the perturbation amplitudes $\zeta_n(t)$ and $\varepsilon_n(t)$. Substituting these resulting relations, together with the pressure conditions [Eqs. (7) and (8)], into Darcy's law [Eqs. (1) and (2)], and consistently keeping terms up to second order, we find the dimensionless equations of motion for the perturbation amplitudes $\zeta_n = \zeta_n(t)$ and $\varepsilon_n = \varepsilon_n(t)$ (for $n \neq 0$),

$$\begin{aligned}
\dot{\zeta}_n &= f_1 \, \Lambda(n)\zeta_n + f_2 \, \Gamma(n)\varepsilon_n \\
&\quad + f_1 \sum_{p \neq 0} [F(n, p)\zeta_p\zeta_{n-p} + G(n, p)\dot{\zeta}_p\zeta_{n-p}] \\
&\quad + f_2 \sum_{p \neq 0} [H(n, p)\varepsilon_p\varepsilon_{n-p} + I(n, p)\dot{\varepsilon}_p\varepsilon_{n-p} \\
&\quad + J(n, p)\dot{\varepsilon}_p\zeta_{n-p}]
\end{aligned} \tag{13}$$

and

$$\begin{aligned}
\dot{\varepsilon}_n &= f_3 \, \Lambda(n)\zeta_n + f_4 \, \Gamma(n)\varepsilon_n \\
&\quad + f_4 \sum_{p \neq 0} [\mathcal{F}(n, p)\varepsilon_p\varepsilon_{n-p} + \mathcal{G}(n, p)\dot{\varepsilon}_p\varepsilon_{n-p}] \\
&\quad + f_3 \sum_{p \neq 0} [\mathcal{H}(n, p)\zeta_p\zeta_{n-p} + \mathcal{I}(n, p)\dot{\zeta}_p\zeta_{n-p} \\
&\quad + \mathcal{J}(n, p)\dot{\zeta}_p\varepsilon_{n-p}],
\end{aligned} \tag{14}$$

where the overdot represents a total time derivative. In Eqs. (13) and (14) lengths and time are rescaled by $L = r_0$ and $T = 12(\eta_1 + \eta_2)r_0^3/\sigma b^2$, respectively, where r_0 is a characteristic length being on the order of the unperturbed radii R_1 and R_2. From this point onward, except as otherwise indicated, we use a dimensionless version of the equations.

The time-independent first-order functions $\Lambda(n)$ and $\Gamma(n)$ are given by

$$
\Lambda(n) = |n|\Bigg\{ \chi \frac{N_{Ba}}{R_1^4} - \chi(1+\chi)N_{Br} - \frac{1}{R_1^3}(n^2 - 1)
$$
$$
- \frac{1}{R_1}\Bigg[S_0 + 3\Upsilon\Bigg(\frac{N_{B_a}}{R_1^2} + N_{B_r}R_1^2 \Bigg)\Bigg]
$$
$$
+ in\chi^2 \mathrm{sgn}(I)\frac{\sqrt{N_{Br}N_{Ba}}}{R_1^2} \Bigg\} \tag{15}
$$

and

$$
\Gamma(n) = |n|\Bigg\{ -\chi \frac{N_{Ba}}{R_2^4} + \chi(1+\chi)N_{Br} - \frac{1}{R_2^3}(n^2 - 1)
$$
$$
- \frac{1}{R_2}\Bigg[S_0 + 3\Upsilon\Bigg(\frac{N_{B_a}}{R_2^2} + N_{B_r}R_2^2 \Bigg)\Bigg]
$$
$$
- in\chi^2 \mathrm{sgn}(I)\frac{\sqrt{N_{Br}N_{Ba}}}{R_2^2} \Bigg\}, \tag{16}
$$

where the sgn function equals ± 1 according to the sign of its argument. We assume that $\mathrm{sgn}(I) = 1$ for an azimuthal magnetic field encircling the current-carrying wire in the counterclockwise direction. In Eqs. (15) and (16) one can identify the contributions from the azimuthal [$\propto N_{Ba}$] and radial [$\propto N_{Br}$] magnetic fields, surface tension [$\propto(n^2 - 1)$], zero-field [$\propto S_0$] and magnetic-field-dependent yield stress [$\propto\Upsilon$], as well as from a complex term that couples the two magnetic field strengths [$\propto\sqrt{N_{Br}N_{Ba}}$]. The expressions for the second-order mode-coupling functions F, G, H, I, J, $\mathcal{F}$, $\mathcal{G}$, $\mathcal{H}$, $\mathcal{I}$, and $\mathcal{J}$ are given in the Appendix [Eqs. (A1)–(A11)].

The system is characterized by several dimensionless parameters:

$$
N_{B_r} = \frac{\mu_0 H_0^2 r_0}{\sigma}, \quad N_{B_a} = \frac{\mu_0 I^2}{4\pi^2 \sigma r_0}, \quad \chi,
$$

$$
S_0 = \frac{3\sigma_{y0} r_0^2}{\sigma b}, \quad \Upsilon = \frac{\alpha r_0}{b\mu_0}, \quad R = \frac{R_1}{R_2}.
$$

The parameters N_{B_r} and N_{B_a} are magnetic Bond numbers that quantify the relative strengths of the radial and azimuthal magnetic field effects to capillary ones, while S_0 refers to the yield stress contributions at zero magnetic field conditions. In addition, Υ characterizes the material properties of the MR fluid being related to the magnetic-field-dependent yield stress [39,45,50]. Finally, R measures the coupling strength between the interfaces of the MR fluid annular ring system: In the limit of a thin (thick) annulus $R \to 1$ ($R \to 0$), the coupling between the inner and outer interfaces is strong (weak). Of course, the annulus cannot be arbitrarily thin, since the effectively two-dimensional Darcy's law approach requires that the Hele-Shaw cell gap thickness b is smaller than any other length scale in the problem [31,32].

The functions

$$
f_1 = \frac{1 + R^{2|n|}}{1 - R^{2|n|}}, \quad f_2 = \frac{2R^{|n|-1}}{1 - R^{2|n|}},
$$
$$
f_3 = \frac{2R^{|n|+1}}{1 - R^{2|n|}}, \quad f_4 = f_1,
$$

that appear in Eqs. (13) and (14) play an important role in the analysis of the physics at play. Note that, as discussed in Ref. [33], under general circumstances (i.e, for $0 < R < 1$), Eqs. (15) and (16) do not express the linear growth rates of the disjoint interfaces. However, in the thick annulus limit ($R \to 0$), $f_1 \to 1$, $f_2 \to 0$, $f_3 \to 0$, and $f_4 \to 1$, and thus Eqs. (13) and (14) decouple. Therefore, only in this weak-coupling limit the functions $\Lambda(n)$ and $\Gamma(n)$ denote the usual, time-independent linear growth rates of the disturbances for the inner and outer interfaces of the MR fluid ring, respectively.

Although our main focus in this work is on nonlinear effects, it is worth pointing out a few important facts that can be extracted at the linear level, in the limit in which the interfaces decoupled: First, note that the azimuthal field destabilizes the inner interface of the annulus, while it stabilizes the outer one. On the other hand, the radial field does just the opposite. Furthermore, the yield-stress contributions act to stabilize both the interfaces. Also, the decoupled linear phase velocities for which mode n, $V_1 = -\mathrm{Im}[\Lambda(n)]/n$ and $V_2 = -\mathrm{Im}[\Gamma(n)]/n$, where $\mathrm{Im}[z]$ stands for the imaginary part of a complex number z, are not dependent on the yield-stress parameters S_0 and Υ. The wave propagation associated to these phase velocities is manifested as rotation of the MR fluid annular droplet. Such a rotational motion is caused by the magnetic normal stresses arising from the combined action of radial and azimuthal magnetic fields [34,39].

Through a linearization process, Livera *et al.* [33] has obtained the time-dependent linear growth rates for both interfaces of a magnetic fluid annulus, yielding

$$
\lambda_1(n, t) \equiv \frac{\dot\zeta_n}{\zeta_n} = f_1 \Lambda(n) + f_2 \Gamma(n)\frac{\varepsilon_n(t)}{\zeta_n(t)} \tag{17}
$$

and

$$
\lambda_2(n, t) \equiv \frac{\dot\varepsilon_n}{\varepsilon_n} = f_1 \Gamma(n) + f_3 \Lambda(n)\frac{\zeta_n(t)}{\varepsilon_n(t)}. \tag{18}
$$

It is worth noting that, in the limit of a thick annulus ($R \to 0$), from Eqs. (17) and (18), we consistently recover the expressions for the linear growth rates derived in previous single-interface studies involving MR fluids in Hele-Shaw cells, subjected to either radial or azimuthal fields, e.g., when a MR fluid that is the outer fluid encircling an inner nonmagnetic fluid drop is perturbed by an applied azimuthal magnetic field [50], and if a MR fluid droplet is surrounded by a nonmagnetic fluid in the presence of a radial field [51,52]. This brief discussion of the linear stability behaviors and related basic equations will help us to better understand the intricacies of the weakly nonlinear results that arise from the solutions of the full-bodied mode-coupling equations (13) and (14), assisted by the auxiliary equations (A1)–(A11).

Equations (13) and (14) constitute one of the central results of this work, offering the time evolution of the perturbation

amplitudes $\zeta_n(t)$ and $\varepsilon_n(t)$ accurate to second order, for the problem of a confined MR fluid annulus enveloped by a non-magnetic fluid, under the action of crossed magnetic fields. As we will verify during the rest of this work, by solving Eqs. (13) and (14) one can get access to key, intrinsically nonlinear behaviors of the MR fluid annular ring, already at the lowest nonlinear, perturbative order. In this way, we will be able to seek various morphological features of interest of the MR annulus, exploring the effects of changes in the dimensionless magnetic yield stress parameter Υ, as well as in the field intensities N_{B_a} and N_{B_r}, and the coupling strength R.

III. EARLY NONLINEAR BEHAVIOR OF THE MR FLUID ANNULUS

For both simply and doubly connected fluid-fluid boundaries involving magnetic-field-induced displacements of ferrofluids and MR fluids in Hele-Shaw cells, usual linear stability analyses fundamentally provide information about the stability of the evolving interfaces with respect to small perturbations [1,32]. Another useful linear input is the prediction of the typical number of interfacial fingered deformations. It is known that, in the linear regime, different interfacial Fourier modes that describe the shape of the perturbed interfaces grow independently of each other, commonly increasing or decaying exponentially as time progresses [33,34,39]. In this purely linear scenario, due to the noninteracting nature of the participating modes, nothing unexpected happens regarding the shape of the resulting fingering structures, and reasonably unstructured fingers are formed. Essentially, the morphology of the linear fingers is merely sinusoidal, and basically determined by the growth of the fastest growing mode.

On the other hand, perturbative mode-coupling analyses show that the consideration of weakly nonlinear contributions introduces nontrivial couplings among the various different interfacial Fourier modes [34,48,49,53–59]. These couplings drive the growth of modes that are not dynamically active in the linear stage. Such emergent modes are in turn responsible for the development of distinctive morphological features of the produced nonlinear patterns. As a consequence of mode coupling, the resulting interfacial lobes can assume a variety of shapes, leading to a much more diverse pattern-forming scheme. Moreover, it has been found that, after a transient purely linear regime, and due to nonlinear effects, the mode amplitudes stop increasing exponentially and eventually saturate [33,34,39]. These nonlinear effects lead to the formation of weakly nonlinear patterns that reach a stationary configuration. As will become clear during the course of this paper, our second-order mode-coupling method offers the possibility to assess various morphological nonlinear features of the confined MR fluid annulus under crossed magnetic fields, including the establishment of stationary patterns.

In this section, we make use of Eqs. (13) and (14), and apply our weakly nonlinear theory to investigate how the magnetic-field-induced rheological properties of the MR fluid annulus impact the shape of the emerging fingering patterns. The main objective of our weakly nonlinear, mode-coupling study is to extract useful physical information about the

complicated pattern-forming dynamics of the system, already at the lowest nonlinear order [i.e., at second order in $\zeta_n(t)$ and $\varepsilon_n(t)$].

Throughout this work, we consider the nonlinear coupling of a finite number N ($N = 40$) of participating Fourier modes: the fundamental mode n, and its harmonics $2n, 3n, \ldots, 40n$. This large number of modes is used to produce annular ring structures having very smooth interfaces. We take the fundamental mode n as given by the closest integer to the fastest growing mode n_{max}, i.e., the mode of maximum linear growth rate at the final time of the evolution $t = t_f$, obtained by the condition $\{d\text{Re}[\lambda_k(n, t_f)]/dn\}|_{n=n_{max}} = 0$, where $\text{Re}[z]$ denotes the real part of a complex number z, and λ_k are given in Eqs. (17) and (18). Note that, since the growth rates $\lambda_1(n, t)$ and $\lambda_2(n, t)$ coincide very quickly for times much smaller than the final times t_f considered, in calculating $n = n_{max}$ one can use either $k = 1$ or $k = 2$ [33].

To generate the nonlinear shapes, we rewrite the complex perturbations $\zeta(\theta, t)$ [$\varepsilon(\theta, t)$] in terms of the real-valued cosine $a_n(t) = \zeta_n(t) + \zeta_{-n}(t)$ [$\bar{a}_n(t) = \varepsilon_n(t) + \varepsilon_{-n}(t)$], and sine $b_n(t) = i(\zeta_n(t) - \zeta_{-n}(t))$ [$\bar{b}_n(t) = i(\varepsilon_n(t) - \varepsilon_{-n}(t))$] amplitudes. With no loss of generality, we set the phase of the fundamental mode so that $a_n > 0$, $\bar{a}_n > 0$, and take the initial conditions $a_n(0) = \bar{a}_n(0) = a_{2n}(0) = \bar{a}_{2n}(0) = \cdots = a_{40n}(0) = \bar{a}_{40n}(0) = 10^{-5}$. Similarly, we consider that $b_n(0) = \bar{b}_n(0) = b_{2n}(0) = \bar{b}_{2n}(0) = \cdots = b_{40n}(0) = \bar{b}_{40n}(0) = 0$. The time evolution of all these mode amplitudes is then obtained by numerically solving the corresponding coupled nonlinear differential equations, given by expressions (13) and (14).

We emphasize that our numerical solutions respect the restrictions imposed by the Darcy-law-based theoretical modeling of the system [31,32]: It does not handle self-intersections of the inner and outer interfaces of the ring (b must be the smallest length scale of the problem), and it obeys conservation of MR fluid annular ring area as time progresses (all fluids involved are incompressible).

A. Dominant radial field

In the framework of this study, it is crucial to figure out how the dimensionless parameters of the problem (N_{Br}, N_{Ba}, χ, S_0, Υ, and R) affect the shape and nonlinear responses of the fingered MR fluid ring-shaped patterns. For the sake of clarity and understanding of the main physical effects involved, and without affecting the validity and relevance of our theoretical analysis, we concentrate our attention on the most influential parameters of the system. Thus, since we are dealing with a MR fluid annulus, we focus on scrutinizing how the material rheological properties of this magnetic fluid (represented by Υ), and the nontrivial coupling between the disjoint, inner and outer interfaces of the annular layer (expressed by R) impact the overall morphology and dynamic behavior of the annular structures. In conjunction with this, we study how the external radial and azimuthal magnetic fields (described by N_{Br} and N_{Ba}) influence the system. This is done for representative values of the remaining dimensionless parameters of the problem (χ and S_0). We stress that, while presenting our theoretical results, we make sure that the values of all relevant dimensionless quantities we utilize are consistent with realistic physical

TABLE I. Summary of key dimensionless parameters.

Parameter	Symbol	Definition	Typical values
Radial magnetic Bond number	N_{B_r}	$\mu_0 H_0^2 r_0/\sigma$	$0 \leqslant N_{B_r} \leqslant 60$
Azimuthal magnetic Bond number	N_{B_a}	$\mu_0 I^2/(4\pi^2 \sigma r_0)$	$0 \leqslant N_{B_a} \leqslant 100$
Magnetic susceptibility	χ	χ	$0.4 \leqslant \chi \leqslant 2$
Yield stress at zero magnetic field	S_0	$3\sigma_{y0} r_0^2/(\sigma b)$	$0 \leqslant S_0 \leqslant 10$
Magnetic-field-dependent yield stress	Υ	$\alpha r_0/(b\mu_0)$	$0 \leqslant \Upsilon \leqslant 1$
Interfacial coupling strength	R	R_1/R_2	$0 \leqslant R \leqslant 0.95$

parameters related to existing Hele-Shaw cell experiments [31,32], magnetic field arrangements [36,38], and material properties of MR fluids [4,5,8,60,61]. Table I summarizes all of the relevant key dimensionless parameters used in our study.

We start our discussion by analyzing how the produced interfacial patterns depend on the leading controlling parameters of the MR fluid annular-ring system: Υ and R. Initially, we focus on cases in which the applied radial magnetic field component is dominant. This is done in Figs. 2–6. In Sec. III B we address the cases in which the azimuthal magnetic field is more intense than its radial counterpart. The reason for concentrating our attention on these two important situations in Secs. III A and III B is the fact that under such circumstances we have been able to find stationary-state MR fluid annular patterns.

Figure 2 displays a typical set of weakly nonlinear MR fluid annular patterns for which $N_{B_r} = 56$ and $N_{B_a} = 20$. In the columns of Fig. 2 the resulting shapes are disposed for three increasing values of the magnetic yield stress parameter: $\Upsilon = 0$ [Figs. 2(a), 2(d), and 2(g)]; $\Upsilon = 0.3$ [Figs. 2(b), 2(e), and 2(h)]; and $\Upsilon = 0.5$ [Figs. 2(c), 2(f), and 2(i)]. In the rows of Fig. 2 the pattern-forming structures are arranged for three values of the coupling strength parameter: $R = 0.6$ [Figs. 2(a)–2(c)]; $R = 0.8$ [Figs. 2(d)–2(f)], and $R = 0.88$ [Figs. 2(g)–2(i)]. We point out that in Fig. 2, as well as in all other figures of this paper that display annular-shaped structures, the patterns shown have already reached a stationary shape for the final times t_f chosen to depict them. In order to give the reader an immediate idea of how the applied magnetic fields relate to the patterns, we also plot a few magnetic field lines (thin lines in Fig. 2).

The final times t_f and fundamental modes $n = n_{\max}$ for the structures portrayed in Fig. 2 are $t_f = 0.012$, $n = 8$ [Fig. 2(a)]; $t_f = 0.022$, $n = 6$ [Fig. 2(b)]; $t_f = 0.05$, $n = 5$ [Fig. 2(c)]; $t_f = 0.013$, $n = 8$ [Fig. 2(d)]; $t_f = 0.03$, $n = 6$ [Fig. 2(e)]; $t_f = 0.08$, $n = 5$ [Fig. 2(f)]; $t_f = 0.014$, $n = 7$ [Fig. 2(g)]; $t_f = 0.047$, $n = 6$ [Fig. 2(h)]; and $t_f = 1.7$, $n = 2$ [Fig. 2(i)]. In all situations of Fig. 2, $R_2 = 1$ and $\chi = 1.5$. Moreover, notice that in Fig. 2, while plotting the various patterns, we keep the outer radius R_2 of the MR fluid annulus fixed. Finally, throughout this work we set the parameter S_0 that expresses the yield-stress contribution in the absence of an applied magnetic field as being zero ($S_0 = 0$). This is done without any loss of generality, since S_0 is usually very small, and only appears at the linear level of the dynamics [see Eqs. (13)-(16) and (A1)–(A11)].

Figures 2(a)–2(c) show how Υ influences the morphology of the annular structures for smaller values of R ($R = 0.6$),

i.e., for situations involving thick annuli. In Fig. 2(a) since $\Upsilon = 0$ and $S_0 = 0$ all yield stress effects vanish, and one has a Newtonian magnetic fluid behavior, leading to the formation of an eightfold polygonal-like annular pattern ($n = n_{\max} = 8$), having a deformed outer boundary, and an almost perfectly circular inner interface. At the outer border of the annulus, one observes the rising of skewed fingers having relatively sharp tips. These peripheral fingers are bent in the direction of the external combined magnetic field **H** (counterclockwise direction), assuming an asymmetric profile. The morphological features of the MR fluid annulus illustrated in Fig. 2(a) for $\Upsilon = 0$ are analogous to the ones shown by equivalent annular ferrofluid shapes studied in Ref. [33]. The asymmetry of the fingers located at the outer interface of the annulus, as identified in Fig. 2(a), is due to the magnetic normal stress associated with the magnetic traction term proportional to $(\mathbf{M} \cdot \hat{\mathbf{n}})^2$ present in the pressure jump boundary conditions [Eqs. (7) and (8)]. This intrinsically nonlinear magnetic traction term induces unequal normal stress on either side of the finger tip profile, breaking its symmetry, and making it bend in the direction of **H**.

Another important magnetically induced feature of the MR fluid annular patterns depicted in Fig. 2 is the fact that these shapes perform a rigid rotational motion. As a matter of fact, we have found that all MR fluid annular structures presented in this section rotate in the counterclockwise direction (i.e., in the direction of the combined field **H**) with a predetermined angular velocity regulated by magnetic effects. Additionally, since all these MR fluid annular morphologies have reached a stationary state, their shapes do remain invariant while they rotate. We refer the reader to the videos provided in the Supplemental Material [62] which clearly illustrate the rotational motion of the patterns displayed in Figs. 2 and 7.

After analyzing Fig. 2(a) for $\Upsilon = 0$, we turn our attention to the action of the parameter $\Upsilon > 0$ on the shape of the MR fluid annular patterns for $R = 0.6$ [Figs. 2(b) and 2(c)]. The most evident shape modification is related to a decrease in the number of fingers arising at the periphery of the annulus when Υ is augmented: while it is $n = n_{\max} = 8$ for $\Upsilon = 0$ in Fig. 2(a), it is reduced to $n = n_{\max} = 6$ ($n = n_{\max} = 5$) for $\Upsilon = 0.3$ ($\Upsilon = 0.5$) in Fig. 2(b) [Fig. 2(c)]. This happens while the shapes of the inner interfaces of the rings in Figs. 2(a)–2(c) remain essentially circular, something that makes sense since the annuli are thick and their interfaces weakly coupled.

Another noteworthy morphological aspect associated with the increase of Υ in Figs. 2(a)–2(c) refers to the shape of the fingered protrusions appearing at the outer interfaces of the annuli: Fig. 2(a) shows an outer boundary crowned by bent spikes, defining fingers that are clearly asymmetric, and
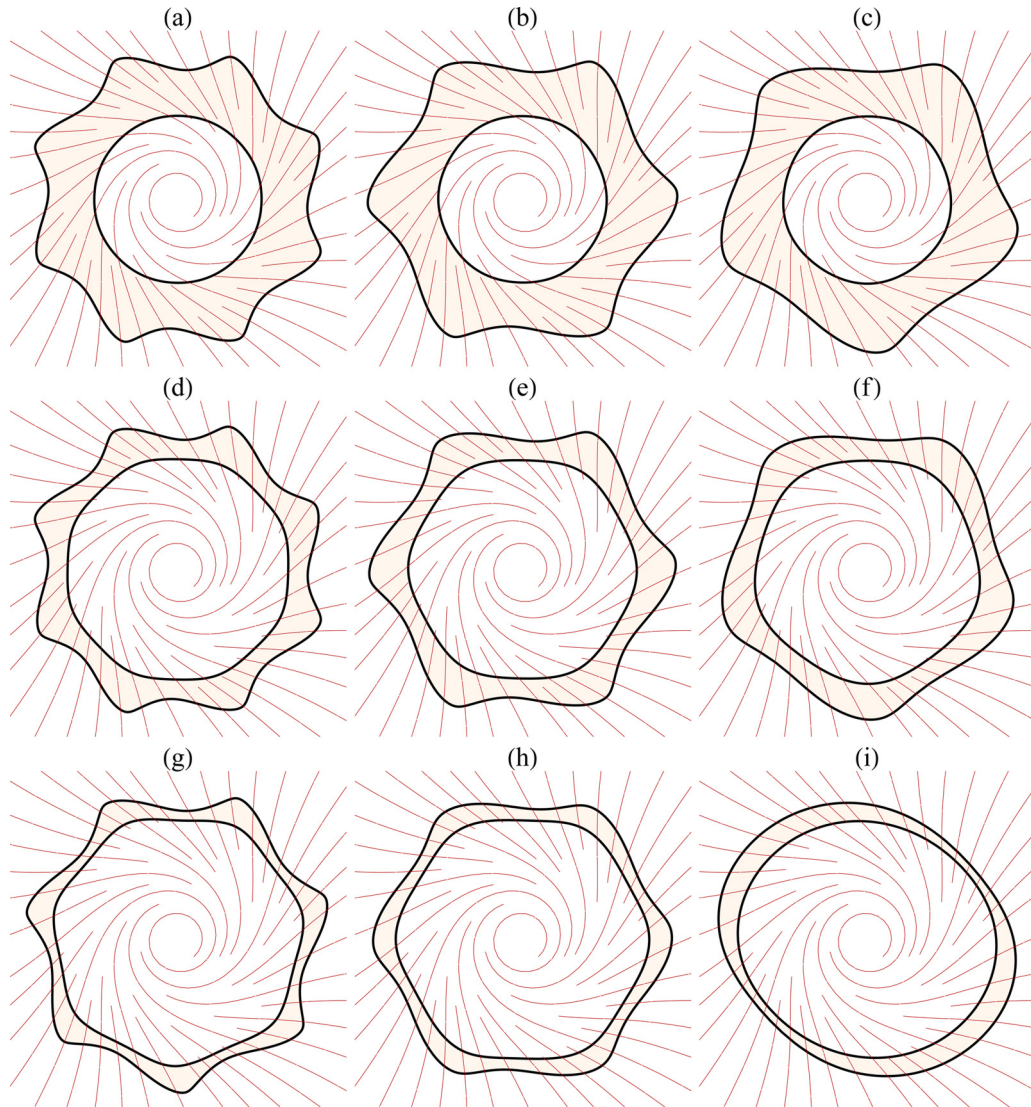
FIG. 2. Representative weakly nonlinear patterns for a confined MR fluid annulus in a crossed magnetic field, where the radial field is dominant. The patterns are obtained for [(a), (d), (g)] $\Upsilon = 0$, [(b), (e), (h)] $\Upsilon = 0.3$, and [(c), (f), (i)] $\Upsilon = 0.5$. In addition, we take [(a)–(c)] $R = 0.6$, [(d)–(f)] $R = 0.8$, and [(g)–(i)] $R = 0.88$. Moreover, $R_2 = 1$, $\chi = 1.5$, $S_0 = 0$, $N_{Br} = 56$, and $N_{Ba} = 20$. In this figure, and in the rest of this work, all depicted annular-ring weakly nonlinear patterns are stationary shapes. To better guide the eye regarding the way the applied magnetic fields relate to the patterns, a few magnetic field lines are also shown.

relatively sharp at their tips. However, for larger Υ [Figs. 2(b) and 2(c)] one observes the formation of fingers that become more and more symmetric, and blunt at their ends. In summary, from the analysis of Figs. 2(a)–2(c) for thick annuli ($R = 0.6$), by increasing the magnetic yield stress parameter Υ one reduces the number of emergent fingers, making them more symmetric in shape, and progressively rounded at their extremities.

Nevertheless, we still have to examine how the basic pattern-forming responses identified in Figs. 2(a)–2(c) stand if one considers thinner MR fluid annuli, and Υ is increased. These behaviors are illustrated in Figs. 2(d)–2(f) for $R = 0.8$, and in Figs. 2(g)–2(i) for $R = 0.88$. The most noticeable feature of these thinner annuli structures is the fact that not only the outer interfaces but also the inner boundaries of the annular ring structures deform. This is due to the stronger coupling between the interfaces for these larger values of the

coupling parameter R. Irrespective of the values of R used, by inspecting Figs. 2(d)–2(f) and Figs. 2(g)–2(i), one finds that the main conclusions reached in Figs. 2(a)–2(c) regarding the role played by increasing Υ remain valid. That is, patterns having a diminished number of more symmetric and less sharp fingers are generated for $R = 0.8$ and $R = 0.88$. It is worth noting the peculiar oval-like shape of the pattern displayed in Fig. 2(i) for the largest values of Υ and R considered in Fig. 2. Actually, we have verified that for yet larger values of Υ and R both the outer and inner interfaces of the MR fluid annulus acquire perfectly circular shapes. It is also pertinent to note the effect of the coupling strength parameter in the sixfold patterns obtained for $\Upsilon = 0.3$ in Figs. 2(b), 2(e), and 2(h) where it is clear that, for a fixed number of fingers ($n = n_{\max} = 6$), larger R increases the bluntness of the fingers. Moreover, by comparing the patterns in Figs. 2(a) and 2(c) with those in Figs. 2(g) and 2(i), we conclude that for a given
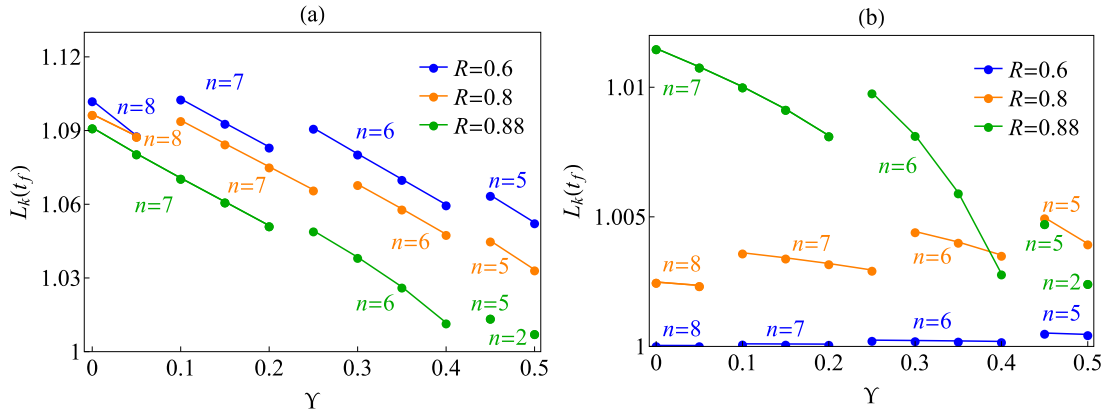
FIG. 3. Normalized interfacial perimeter $L_k(t_f)$ [Eq. (19)] with respect to variations in Υ, for three values of R, corresponding to the situations leading to the patterns illustrated in Fig. 2. The perimeters for the outer interfaces ($k = 2$) of the MR fluid annuli are shown in (a), while the corresponding perimeter values for the inner interfaces ($k = 1$) are plotted in (b). All physical parameters used here are identical to those utilized in Fig. 2. To better guide the eye, in addition to just considering $\Upsilon = 0$, 0.3, and 0.5 as in Fig. 2, a few extra values of Υ have been included. The values of the fundamental modes $n = n_{\max}$ for each case are also indicated.
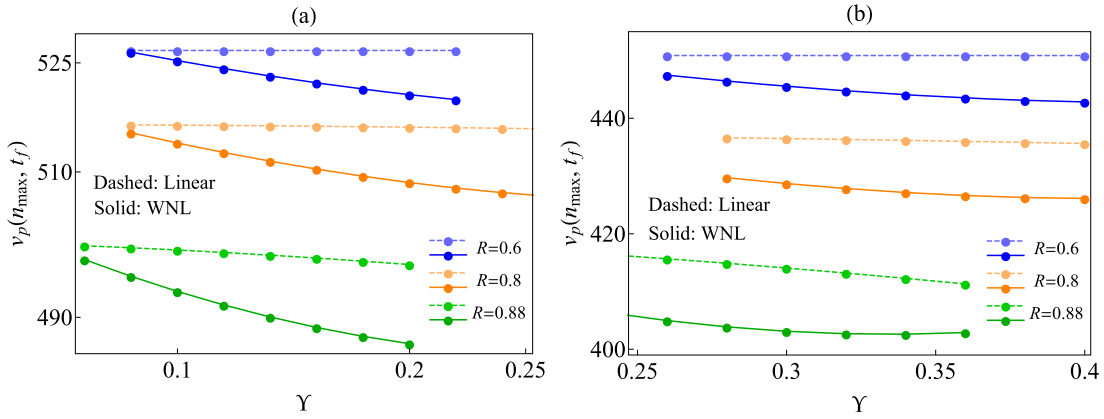
FIG. 4. Variation of the phase velocity $v_p(n_{\max}, t_f)$ with the magnetic yield stress parameter Υ, for (a) $n_{\max} = 7$ and (b) $n_{\max} = 6$. The linear (dashed lines) and weakly nonlinear (solid lines) cases are considered, by taking $R = 0.6$, 0.8, and 0.88. The other physical parameters utilized in this figure are identical to the ones used in Fig. 2.
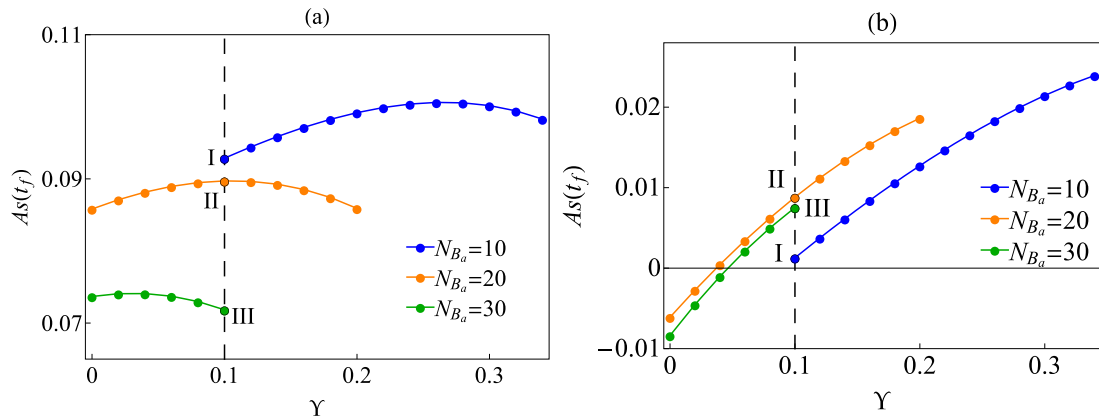
FIG. 5. Asymmetry function $As(t)$ [Eq. (22)] evaluated at the final time $t = t_f$, plotted in terms of Υ for three values of the azimuthal magnetic Bond number N_{Ba}. This is done for the (a) outer and (b) inner interfaces of a MR fluid annulus for which $n_{\max} = 7$ and $R = 0.88$. The weakly nonlinear annular ring shapes corresponding to points I, II, and III given by the intersection of the vertical dashed lines at $\Upsilon = 0.1$ with the curves for the three N_{Ba} considered are presented in Fig. 6. The remaining physical parameters used in this figure are equal to those set in Fig. 2.
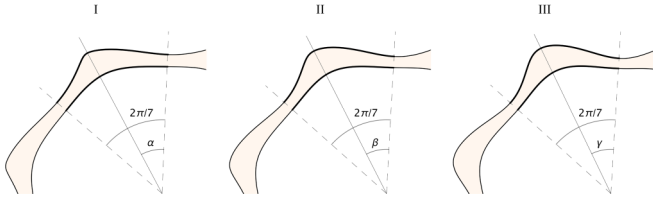
FIG. 6. Close-up view of representative weakly nonlinear interfacial annular structures for the outer and inner boundaries of the MR fluid patterns that arise at points I, II, and III in Fig. 5 for $\Upsilon = 0.1$. The angular sector delimited by the dashed lines is given by $\varphi = 2\pi/7$. Moreover, in I, $\alpha = 58.9\%$ of φ, in II, $\beta = 58.5\%$ of φ, and in III, $\gamma = 56.7\%$ of φ. This indicates that the fingers located at the outer interface of the annulus become less asymmetric for larger values of N_{Ba}.

value of Υ, larger values of R provoke a reduction in the number of fingers. In summary, the results displayed in Fig. 2 demonstrate that by manipulating the material properties of the MR fluid (Υ) and the thickness of the annuli (R) one can conveniently adjust and design the shape of the resulting patterns.

After discussing the most characteristic morphological properties of the MR fluid annular patterns presented in Fig. 2, we continue our investigation by performing a more quantitative evaluation of the stability behavior of the inner and outer boundaries of the annular ring structures, when Υ and R are varied. A convenient and simple way to assess the degree of stability (or instability) of the inner and outer boundaries of the annuli is provided by examining the behavior of the perimeter of such interfaces as a function of Υ, for a few values of R. This is shown in Fig. 3 which plots the normalized perimeter of the limiting interfaces of the MR fluid annulus at the final time,

$$L_k(t_f) = \frac{1}{2\pi R_k} \int_0^{2\pi} \sqrt{\mathcal{R}_k^2(t_f) + \left[\frac{d\mathcal{R}_k(t_f)}{d\theta}\right]^2} \, d\theta, \quad (19)$$

where the subscript $k = 1$ ($k = 2$) labels the inner (outer) interface of the annular ring structure. The results shown in Fig. 3 use the same parameters used to get the patterns exhibited in Fig. 2, and also include a few additional values of Υ. More specifically, Fig. 3 illustrates how the normalized perimeter $L_k(t_f)$ varies as a function of Υ, for the three values of R utilized in Fig. 2, for the outer $k = 2$ [Fig. 3(a)] and inner $k = 1$ [Fig. 3(b)] interfaces of the MR fluid annular structures.

The more quantitative results presented in Fig. 3 confirm some of the visually based conclusions we have reached from our discussion of Fig. 2. By examining Fig. 3 it is apparent that, for given values of R and $n = n_{max}$, larger values of Υ tend to produce more stable inner and outer annular ring interfaces, that have smaller perimeters and a reduced number of fingers. It is also evident that variations of the perimeters with Υ are more intense for the outer interfaces of the MR fluid annulus [note the different ranges in the vertical axes of Figs. 3(a) and 3(b)]. This makes sense, since the more prevalent effects come from the radial magnetic field component which tends to make the outer interface more unstable than the inner one.

At this point, we examine how the parameters Υ and R influence the phase velocity $v_p(n, t)$ associated with the rotational motion of the MR fluid annulus caused by the crossed magnetic field. Figure 4 plots the weakly nonlinear (WNL) phase velocities of the fundamental mode $n = n_{max}$ at the final time $t = t_f$ (solid lines),

$$v_p(n, t) = -\frac{1}{n} \text{Im}\left[\frac{\dot{\zeta}_n(t)}{\zeta_n(t)}\right] = -\frac{1}{n} \text{Im}\left[\frac{\dot{\varepsilon}_n(t)}{\varepsilon_n(t)}\right], \quad (20)$$

which are numerically evaluated by using Eqs. (13) and (14). Figure 4 also depicts the linear phase velocities for $n = n_{max}$ at $t = t_f$ (dashed lines),

$$v_p(n, t) = -\frac{1}{n} \text{Im}\left[\lambda_1(n, t)\right] = -\frac{1}{n} \text{Im}\left[\lambda_2(n, t)\right], \quad (21)$$

where $\lambda_1(n, t)$ [$\lambda_2(n, t)$] is given by Eq. (17) [Eq. (18)]. The coupled-interface, linear phase velocities expressed in Eq. (21) should not be confused with the decoupled phase velocities $V_1 = -\text{Im}[\Lambda(n)]/n$ and $V_2 = -\text{Im}[\Gamma(n)]/n$ presented in Sec. II when we discussed the thick annulus limit ($R \to 0$) in which the inner and outer interfaces do not interact. Equations (20) and (21) express the fact that, after the pattern reaching a stationary state, both the inner and the outer interfaces of the MR fluid ring have the same phase velocities (i.e., the shape of the MR fluid annulus remains immutable during its rotation).

Figure 4 displays the variation of the linear and weakly nonlinear phase velocities $v_p(n_{max}, t_f)$ for a few values of magnetic yield stress parameter Υ, for the same values of the coupling parameter R used in Fig. 2 ($R = 0.6$, 0.8, and 0.88), and for two representative values of the fundamental mode, $n_{max} = 7$ [Fig. 4(a)] and $n_{max} = 6$ [Fig. 4(b)]. The remaining parameters are identical to those used in Fig. 2. Among the data shown in Fig. 4 one can find the behaviors of the sixfold and sevenfold patterns portrayed in Fig. 2. First of all, observe that the values of the phase velocities shown are positive, indicating that all MR fluid annular patterns rotate in the same direction as the external combined magnetic field **H** (i.e., in the counterclockwise direction). Additionally, by going through the data presented in Figs. 4(a) and 4(b), one readily notices that the solid lines always lie below the dashed ones. This means that nonlinear mode-coupling effects introduce a correction in the values of the phase velocities predicted by the linear theory, decreasing their magnitudes. From Figs. 4(a) and 4(b) is its also apparent that for lower values of R ($R = 0.6$ and $R = 0.8$), while the linear phase velocities remain unchanged as Υ is varied, the WNL phase velocities decrease as Υ assumes larger values. Nonetheless, for a higher value of the coupling parameter R ($R = 0.88$), both the linear and WNL velocities diminish as Υ is increased. For $R = 0.88$ one can also notice that the WNL prediction results in stronger variations of the phase velocity as Υ is augmented than the ones predicted by the linear theory. These results strengthen the relevance of performing a weakly nonlinear mode-coupling analysis for the MR fluid annular problem under crossed magnetic fields. After all, from Fig. 4 one can verify that the WNL approach offers important corrections to the purely linear prediction for phase velocity v_p as the controlling parameters Υ and R are modified.
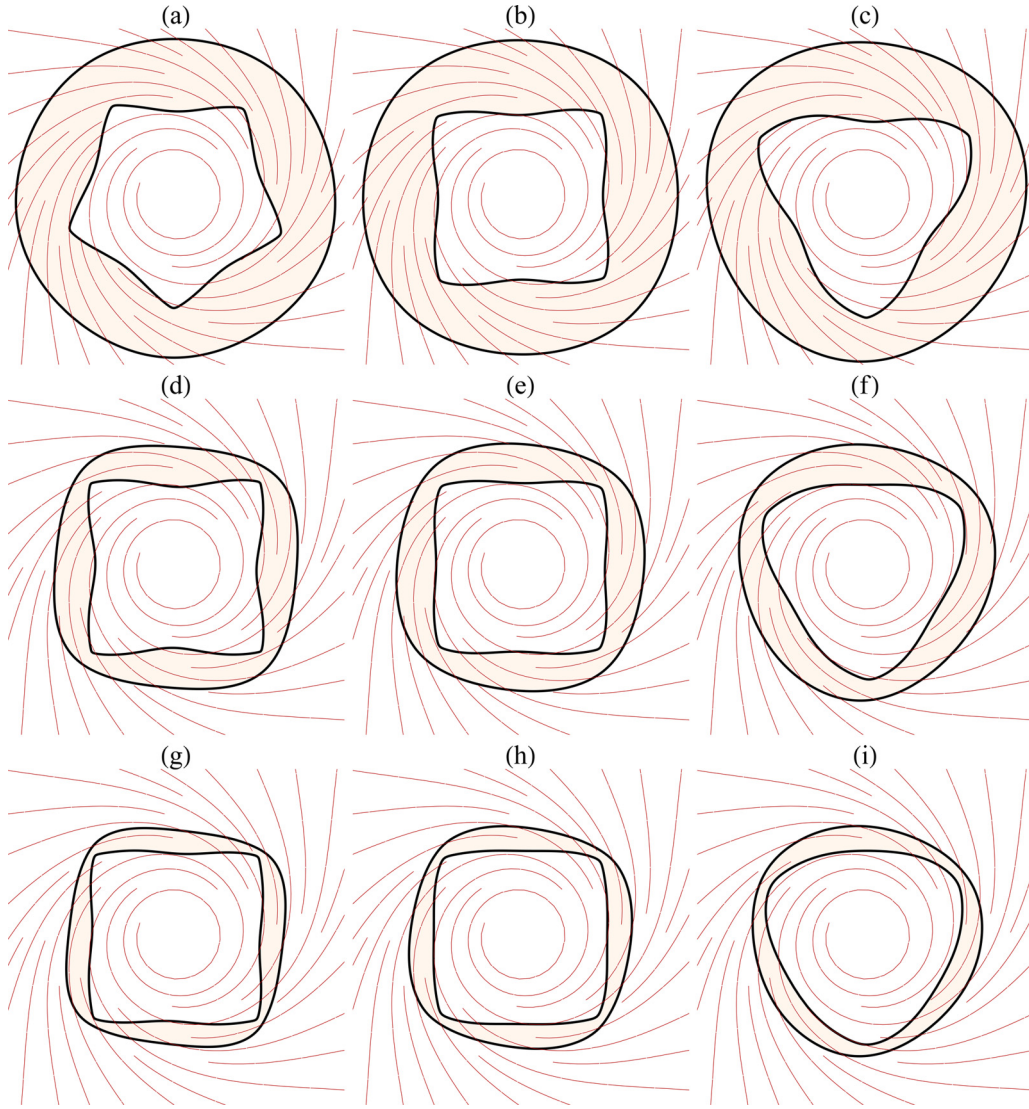
FIG. 7. Typical examples of weakly nonlinear, stationary patterns for a confined MR fluid annular ring in a crossed magnetic field, when the azimuthal magnetic field is dominant. The patterns are produced for [(a), (d), (g)] $\Upsilon = 0$, [(b), (e), (h)] $\Upsilon = 0.05$, and [(c), (f), (i)] $\Upsilon = 0.12$. The values of the coupling strength parameter are [(a)–(c)] $R = 0.6$, [(d)–(f)] $R = 0.75$, and [(g)–(i)] $R = 0.835$. Additionally, $R_1 = 1$, $\chi = 0.75$, $S_0 = 0$, $N_{Ba} = 100$, and $N_{Br} = 5$. As we did in Fig. 2, a few applied magnetic field lines are also plotted.

As commented earlier in this work, one of the most conspicuous behaviors of magnetic fluid annular systems under the action of the combined magnetic field **H** [Eq. (3)] is the fact that the ring-shaped structures rotate in the direction **H**, making the emergent fingers turn also in the direction of **H**. This leads to the formation of bent interfacial fingered lobes having asymmetric profiles. We close our analysis of the situation in which the radial field is dominant by discussing Figs. 5 and 6. In Fig. 5 we examine how the asymmetric shape of the fingers that arise in the outer [Fig. 5(a)] and inner [Fig. 5(b)] interfaces of the MR fluid annulus responds to variations on the magnetic yield stress parameter Υ. This is investigated by considering three values of the azimuthal Bond number, $N_{Ba} = 10$, 20, and 30, whereas the radial Bond number is kept fixed. As in Fig. 2 we take $N_{Br} = 56$. The representative situations shown in Fig. 5 concentrate on the behavior of the fingers for thin ($R = 0.88$), sevenfold ($n = n_{\max} = 7$) MR fluid annular patterns, like the one depicted in Fig. 2(g).

To quantify the asymmetry of the fingers, we follow Refs. [34,63,64] and introduce the asymmetry function

$$As(t) = \frac{\langle \mathcal{H}[\xi]^3 \rangle}{\langle \xi^2 \rangle^{3/2}}, \tag{22}$$

where $\langle \cdot \rangle = \frac{1}{2\pi} \int_0^{2\pi} (\cdot) d\theta$, $\mathcal{H}[\cdot]$ is the Hilbert transform, and $\xi = \zeta(\theta, t)$ [$\xi = \varepsilon(\theta, t)$] for the inner (outer) interface of the annular ring structure. The fingers tilt in the counterclockwise (clockwise) direction if $As(t) > 0$ [$As(t) < 0$]. Figure 5 shows how the asymmetry function evaluated at the final time $t = t_f$, $As(t_f)$, varies with Υ for three values of N_{Ba}, for the outer [Fig. 5(a)] and inner [Fig. 5(b)] interfaces of the MR fluid annulus. It is considered that $n_{\max} = 7$ and $R = 0.88$.

From the data illustrated in Fig. 5(a) for the outer interface of the MR fluid annulus, one can verify that for a given Υ, the larger the azimuthal magnetic Bond number N_{Ba} the smaller

the finger asymmetry. This is exemplified by the points I, II, and III given by the intersections of the vertical dashed line for $\Upsilon = 0.1$ with the curves of $As(t_f)$ for the three chosen values of N_{Ba}. On the other hand, for a specific N_{Ba} and as Υ is increased, one can also see that the function $As(t_f)$ behaves nonmonotonically with Υ: after an initial increase, the function reaches a maximum, and then falls off. This indicates that for a given N_{Ba} one can conveniently tune Υ in such a way that the finger asymmetry is maximized, or minimized. It should be mentioned that these conclusions are valid for the whole interval $10 \leqslant N_{Ba} \leqslant 30$. On the other hand, for smaller values of N_{Ba} (i.e., for $0 \leqslant N_{Ba} \leqslant 10$), not shown in Fig. 5, we have also identified other possible behaviors: For example, when $N_{Ba} = 0$ the fingers emerging at the outer interface of the annulus are perfectly symmetric, whereas for $0 < N_{Ba} \leqslant 10$ the asymmetry function $As(t_f)$ increases with increasing Υ.

The analysis of the asymmetry of the fingers that arise in the inner interface of the MR fluid annulus is not as simple as for the outer interface fingers. First, by inspecting the vertical axes of Figs. 5(a) and 5(b) one realizes that magnitudes of the asymmetry function $As(t_f)$ for the outer interface are considerably larger than the ones obtained for the inner boundary of the MR fluid ring. This means that for the cases we are currently investigating, finger asymmetry effects are much more easily observable at the outer interface. Although these asymmetry effects are less intense, they are still of interest, as displayed in Fig. 5(b). The most remarkable feature detected in Fig. 5(b) is the fact that for $N_{Ba} = 20$ and 30 the function $As(t_f)$ changes sign as Υ is increased. Thus, in these cases, even though the MR fluid annulus rotates in the counterclockwise direction (i.e., in the direction of **H**), depending on the value of Υ, the fingers can tilt either in the clockwise [for $As(t_f) < 0$] or in the counterclockwise direction [for $As(t_f) > 0$]. However, as it will become evident in Fig. 6, this appealing behavior is very hard to be pictorially observed at the weakly nonlinear level.

To illustrate a bit more vividly some of the aspects about the asymmetry of the fingers described in Fig. 5, we present Fig. 6. In Fig. 6 we portray the interfacial annular patterns that arise at points I, II, and III indicated in Fig. 5. In order to facilitate the visualization of the morphological details of the resulting fingering structures, instead of plotting the entire annular pattern, we show a close-up view of part of the annulus, focusing on an angular sector of aperture $\varphi = 2\pi/7$ (delimited by dashed lines), near one of the fingered projections. For the reasons pointed out above, we aim attention at the fingers located at the outer interface of the annulus. Notice that in Fig. 6 the aforementioned angular sector is limited by two dashed lines connecting the center of the annulus to the two local minima of the outer interface. On the other hand, the solid line joins the center of the ring to the local maximum of the outer interface. For a perfectly symmetric finger, the angle defined by the solid line and one of the dashed lines would be 50% of φ, or simply $\pi/7$. However, for the structures depicted in Fig. 6 we have that in I, $\alpha = 58.9\%$ of φ, in II, $\beta = 58.5\%$ of φ, and in III, $\gamma = 56.7\%$ of φ. These more visually evident findings are consistent with the data points I, II, and III indicated in Fig. 5(a) for $\Upsilon = 0.1$, implying that the fingers of the outer interface become less asymmetric as N_{Ba} is increased. These results are also compatible with the

fact that the azimuthal magnetic field tends to stabilize the outer interface of the the magnetic fluid annulus, as discussed in Sec. II.

Performing similar measurements for the inner interfaces yields in I, $\alpha = 50.28\%$ of φ, in II, $\beta = 50.98\%$ of φ, and in III, $\gamma = 50.77\%$ of φ, being also in line with the data points I, II, and III portrayed in Fig. 5(b) for $\Upsilon = 0.1$. Therefore, for fixed values of Υ and N_{Br}, the azimuthal magnetic field component can be used to control the asymmetry of the fingers formed at the outer and inner borders of the MR fluid annulus.

B. Dominant azimuthal field

In this section, we direct our attention to cases in which the effect of the azimuthal magnetic field component of the crossed magnetic field **H** dominates over the one provoked by the radial component of **H**. This is done in Figs. 7–11.

We initiate our analysis by presenting in Fig. 7 a characteristic collection of possible MR fluid annular patterns for which $N_{Ba} = 100$ and $N_{Br} = 5$. In addition, we have that $R_1 = 1$ and $\chi = 0.75$. As in Sec. III A, for all situations studied in this section we set $S_0 = 0$. In the columns of Fig. 7 the patterns are exhibited for three increasing values of the magnetic yield stress parameter: $\Upsilon = 0$ [Figs. 7(a), 7(d), and 7(g)], $\Upsilon = 0.05$ [Figs. 7(b), 7(e), and 7(h)], and $\Upsilon = 0.12$ [Figs. 7(c), 7(f), and 7(i)]. In the rows of Fig. 7 the ring-shaped structures are arranged for three magnitudes of the coupling strength parameter: $R = 0.6$ [Figs. 7(a)–7(c)]; $R = 0.75$ [Figs. 7(d)–7(f)], and $R = 0.835$ [Figs. 7(g)–7(i)]. The stationary shapes depicted in Fig. 7 are taken for the final times t_f, and fundamental modes $n = n_{\max}$ given by $t_f = 0.06$, $n = 5$ [Fig. 7(a)]; $t_f = 0.09$, $n = 4$ [Fig. 7(b)]; $t_f = 0.22$, $n = 3$ [Fig. 7(a)]; $t_f = 0.08$, $n = 4$ [Fig. 7(d)]; $t_f = 0.10$, $n = 4$ [Fig. 7(e)]; $t_f = 0.23$, $n = 3$ [Fig. 7(f)]; $t_f = 0.10$, $n = 4$ [Fig. 7(g)]; $t_f = 0.11$, $n = 4$ [Fig. 7(h)]; and $t_f = 0.48$, $n = 3$ [Fig. 7(i)]. Note that while plotting Fig. 7, we keep the inner radius R_1 fixed, so when we increase the value of $R = R_1/R_2$, the outer radius R_2 becomes smaller. This is the reason why the annular patterns shown in Fig. 7 look smaller when larger R are taken.

The essential features of the patterns in Fig. 7 can be classified as follows. The most evident aspect of the annular structures generated under dominant azimuthal field conditions is the fact that the strongest interfacial perturbations occur at the inner boundary of the ring. Such a weakly nonlinear observation is in consonance with our discussion performed in Sec. II, where we have seen that the azimuthal magnetic field component tends to destabilize (stabilize) the inner (outer) interface of the MR fluid annulus. By the way, note that such a nonlinear feature exhibited in Fig. 7 is true irrespective of the values of Υ and R considered. This emblematic visual facet of the patterns in Fig. 7 is clearly in contrast to what has been seen in Fig. 2, when the radial field is the prevalent one. In the situations depicted in Fig. 2, the more intense deformations take place at the outer border of the annulus. Another particularity of the annular-ring shapes illustrated in Fig. 7 refers to the conformation of the structures formed at the inner boundary: one observes the rising of polygonal-like, n-fold patterns having tips (vertices) and edges of different formats. An additional characteristic of the inner interfaces is that, for a given R, and as Υ is in-
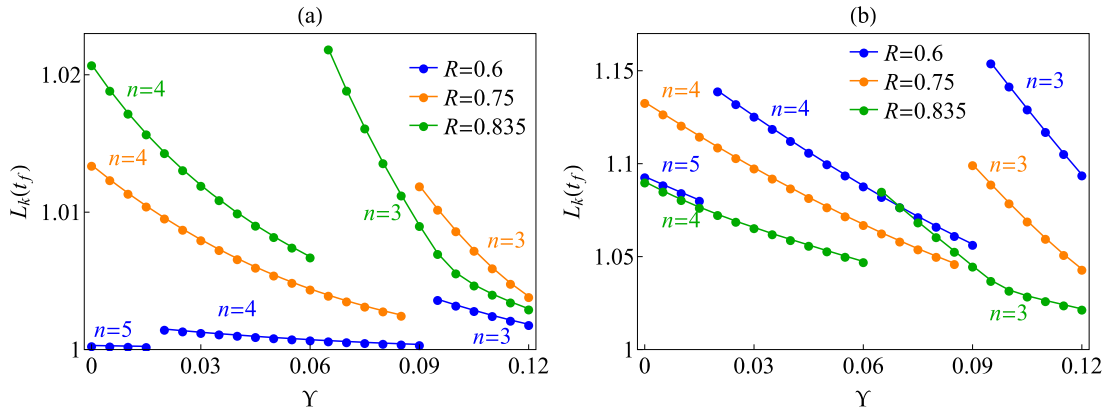
FIG. 8. Normalized interfacial perimeter $L_k(t_f)$ [Eq. (19)] plotted as a function of Υ, for three values of R, corresponding to cases associated with the annular shapes portrayed in Fig. 7. The perimeters for the outer interfaces ($k = 2$) of the MR fluid annuli are depicted in (a), while the equivalent perimeter values for the inner interfaces ($k = 1$) are shown in (b). All physical parameters utilized here are equal to those used in Fig. 7. To facilitate visualization of the data, in addition to just including $\Upsilon = 0$, 0.05, and 0.12 as in Fig. 7, a few additional values of Υ are provided. The values of the fundamental modes $n = n_{\max}$ for each case are also given.
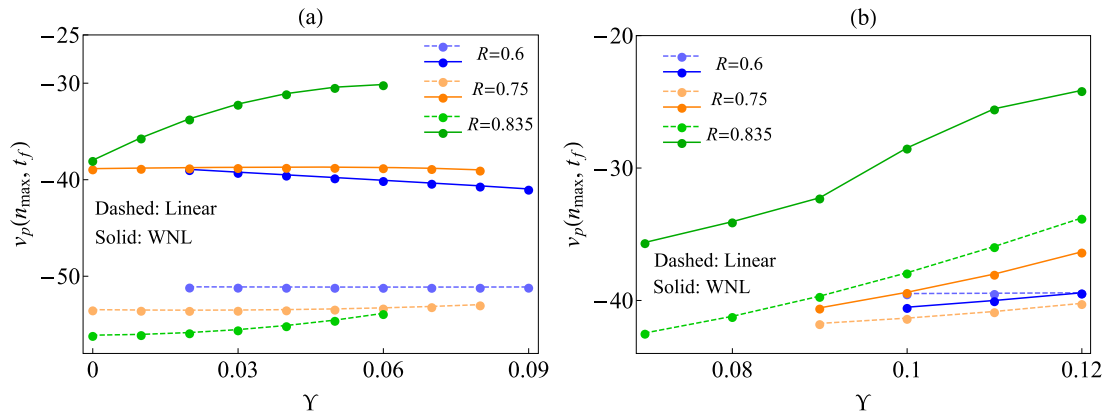
FIG. 9. Behavior of the phase velocity $v_p(n_{\max}, t_f)$ of the fundamental mode $n = n_{\max}$ at time $t = t_f$ as the magnetic yield stress parameter Υ is modified, for (a) $n_{\max} = 4$, and (b) $n_{\max} = 3$. The linear (dashed lines) and weakly nonlinear (solid lines) cases are displayed, by considering three values of the coupling strength parameter $R = 0.6$, 0.75, and 0.835. The remaining physical parameters used in this figure are equal to those employed in Fig. 7.
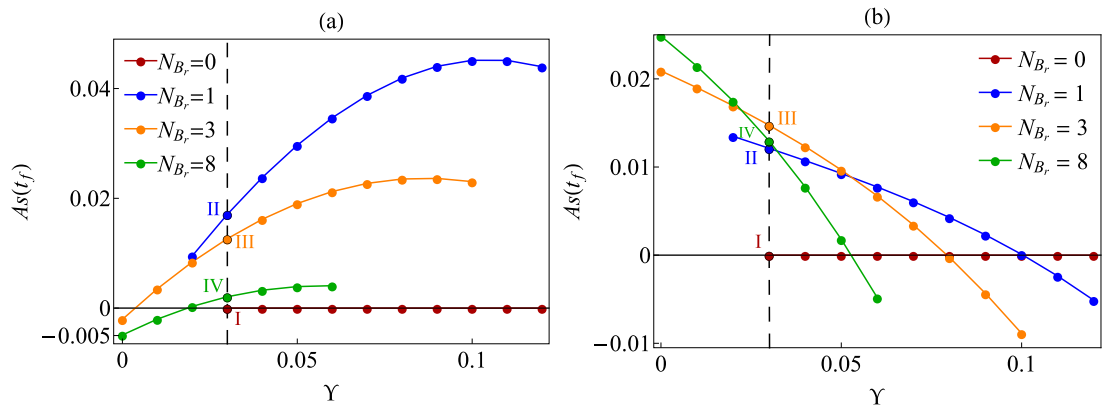
FIG. 10. Asymmetry function $As(t)$ [Eq. (22)] at the final time $t = t_f$, plotted as a function of Υ for increasing values of the radial magnetic Bond number N_{B_r}: 0, 1, 3, and 8. The data for the (a) outer and (b) inner interfaces of the annulus are shown considering that $n_{\max} = 4$ and $R = 0.75$. The weakly nonlinear annular patterns corresponding to points I, II, III, and IV given by the intersection of the vertical dashed lines at $\Upsilon = 0.03$ with the curves for the four N_{B_r} of interest are displayed in Fig. 11. The other physical parameters utilized in this figure are the same as the ones used in Fig. 7.
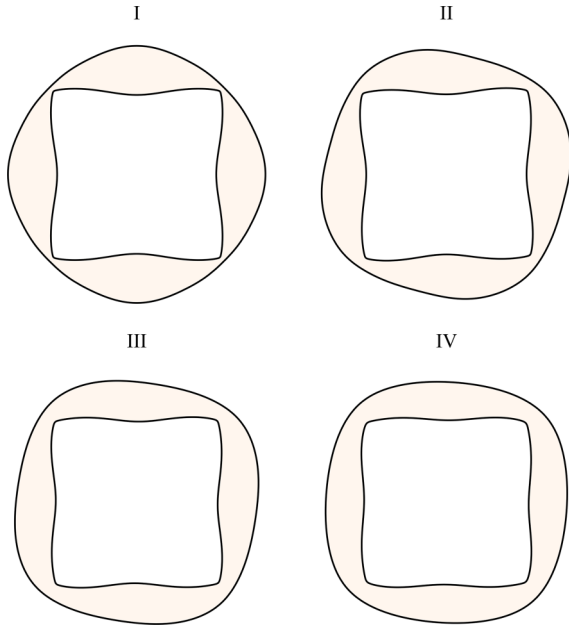
FIG. 11. Representative weakly nonlinear MR fluid annular patterns that arise at points I, II, III, and IV in Fig. 10 for $\Upsilon = 0.03$.

creased, one identifies an enhanced stabilization of the internal polygonal structures, and a tendency toward a reduction on the number of generated fingers. Under such circumstances, the vertices tend to change from thin and sharp to wide and blunt, and edges vary from concave to convex. Furthermore, it is quite clear that the outer interfaces become progressively deformed for higher values of R due to the stronger coupling with the inner boundaries of the annuli. It is also worthwhile to note that as Υ and R are modified, the annular structures can reveal some degree of misalignment between the inner and outer interfaces, signaling the presence of interfacial asymmetry. For instance, by inspecting Figs. 7(b), 7(e), and 7(h) for $\Upsilon = 0.05$, one can see that the outer interfaces become more asymmetric for larger values of R. Therefore, from Fig. 7 one can verify that by appropriately adjusting the values of the controlling parameters Υ and R one can construct a variety of MR fluid annular patterns having different shapes, thicknesses, and symmetry properties.

Similar to what we did in Sec. III A, after the presentation of the characteristic pattern-forming structures that arise under the condition in which the azimuthal magnetic field component is dominant (Fig. 7), we proceed by exploiting in a more quantitative fashion some of their most important behaviors. More specifically, we are interested in examining how the morphology of the patterns, their stability, number of fingers, phase velocities, and asymmetry properties respond to variations in the most important governing parameters of the system, namely, Υ and R.

Figure 8 shows how the normalized interfacial perimeter $L_k(t_f)$ [Eq. (19)] varies with Υ, for the three values of the coupling strength parameter R used in Fig. 7: 0.6, 0.75, and 0.835. $L_k(t_f)$ is measured both for the outer $(k = 2)$ [Fig. 8(a)], and inner $(k = 1)$ [Fig. 8(b)] interfaces of the annular ring structures. The results illustrated in Fig. 8 utilize the same parameters used to generate the patterns exhibited

in Fig. 7, but also include data for a few additional values of Υ.

By observing Fig. 8 one readily notices that regardless of the values of $n = n_{\max}$ and R, and both for the outer [Fig. 8(a)] and inner [Fig. 8(b)] interfaces, $L_k(t_f)$ decreases as Υ increases. Furthermore, in contrast to what we have seen in Fig. 3, note that in Fig. 8 the perimeters of the inner interfaces are larger than the perimeters of the corresponding outer interfaces. In general, for the outer interfaces [Fig. 8(a)], which tend to become increasingly unstable when the coupling between the interfaces of the annuli is more intense, it makes sense that higher values of R tend to lead to larger perimeters [see, for example, the curves for $n = 4$ in Fig. 8(a)]. However, a different behavior can also be observed: For instance, for the curves related to $n = 3$ in Fig. 8(a), this is not true. As the instabilities on the outer interface are mostly induced by the coupling with the inner one, a more stable inner interface will lead to a more stable outer interface. For example, by examining Fig. 7 one can see that the inner interface for $R = 0.835$ [Fig. 7(i)] is less deformed than the inner one for $R = 0.75$ [Fig. 7(f)]. Therefore, even though the coupling is larger, the outer interface in Fig. 7(i) is less deformed than the outer interface in Fig. 7(f). Finally, from Fig. 8(b) one verifies that the behavior of the perimeters of the inner interfaces with R is quite robust, and for all $n = n_{\max}$ one can see that larger values of R consistently lead to smaller $L_k(t_f)$. This can be justified as follows. As the inner interface couples with the outer one to destabilize it, the outer interface interacts back, but trying stabilize the inner one (recall that larger azimuthal fields tend to stabilize the outer border of the annulus). This finding from Fig. 8(b) agrees with the behavior of the inner interfaces seen in Figs. 7(b), 7(e), and 7(h) for $n = 4$, and Figs. 7(c), 7(f), and 7(i) for $n = 3$.

We advance by examining how the phase velocity $v_p(n_{\max}, t_f)$ behaves as Υ is varied, for $R = 0.6$, 0.75, and 0.835 (Fig. 9). This is done for $n_{\max} = 4$ [Fig. 9(a)] and $n_{\max} = 3$ [Fig. 9(b)]. The solid lines represent the WNL phase velocities given by Eq. (20), while the dashed lines express the linear phase velocities calculated by Eq. (21). The rest of the physical parameters used to plot Fig. 9 are the same as the ones used in Fig. 7.

One remarkable point about Fig. 9 refers to the sign of phase velocity. By scrutinizing Fig. 9, one immediately verifies that $v_p(n_{\max}, t_f)$ is negative for all values of the parameters. This means that under the circumstances studied in this section, i.e., dominant azimuthal magnetic field, the stationary state MR fluid annular patterns pictured in Fig. 7 rotate in the clockwise direction (see the Supplemental Material [62]), in opposition to the (counterclockwise) direction of the combined magnetic field **H**. This should be contrasted with the behaviors of the patterns shown in Fig. 2 for the case in which the radial magnetic field component is dominant, whose patterns rotate in the counterclockwise direction, as demonstrated in Fig. 4 where $v_p(n_{\max}, t_f) > 0$. Therefore, as it was the case for ferrofluid annular rings in crossed magnetic fields [33], by changing the relative intensity of radial and azimuthal magnetic field components, one is able to control the direction of rotation of the MR fluid structures. On top of this, in the case of MR fluid annular structures, we found an extra capability: in addition to the direction of rotation, one

can tune the magnitude of the phase velocities by properly adjusting the values of the controlling parameters Υ and R. This is clearly seen in Figs. 9(a) and 9(b). By paying attention to the solid lines (WNL results), one notices that for a given Υ the phase velocities increase with growing R. On the other hand, for a given R the phase velocities can either increase or decrease as Υ assumes larger values. Thus, in the case of MR fluid annulus under crossed magnetic fields, by changing the strength of the applied field components, as well as the values of the magnetic yield stress Υ and the coupling parameter R, one is able to control the direction and magnitude of the phase velocity (or, equivalently, the angular velocity) of the stationary patterns. Another noteworthy point revealed by Fig. 9 is the fact that in most of the situations outlined, there is a considerable difference between the WNL (solid lines) and linear (dashed lines) predictions for the phase velocities, indicating that in general the WNL approach predicts phase velocities whose magnitudes are smaller than the values estimated by the purely linear theory.

We close this section by analyzing Figs. 10 and 11. Figure 10 illustrates how the asymmetry function $As(t)$ [Eq. (22)] at the final time $t = t_f$ varies with Υ for growing values of the radial magnetic Bond number N_{Br}: 0, 1, 3, and 8. We set $n_{max} = 4$, $R = 0.75$, and describe the behavior of $As(t)$ for the outer [Fig. 10(a)] and inner [Fig. 10(b)] boundaries of the MR fluid annular ring. The rest of the physical parameters used in Figs. 10 and 11 are the identical to those applied in Fig. 7.

First, from the inspection of Figs. 10(a) and 10(b) it is apparent that when $N_{Br} = 0$, both the outer and the inner interfaces are entirely symmetric, meaning that $As(t_f) = 0$ for all values of the magnetic yield stress parameter Υ. This is reasonable, since interfacial asymmetry only arises if both azimuthal and radial fields are nonzero (see Sec. II). It is also clear from Fig. 10(a) that for the outer interface and for $N_{Br} \geqslant 1$, asymmetry tends to increase as Υ is increased. However, for larger values of Υ the asymmetry function eventually reaches a maximum, and then starts to decrease. Moreover, for a fixed value of Υ in Fig. 10(a) (e.g., for $\Upsilon = 0.03$, identified by a vertical dashed line), the asymmetry tends to decrease as N_{Br} is augmented [see points II, III, and IV indicated in Fig. 10(a)]. A more pictorial account about this last observation can be seen by examining the outer interfaces of the patterns I, II, III, and IV portrayed in Fig. 11, which are the resulting annular structures corresponding to points I, II, III, and IV shown in Figs. 10(a) and 10(b). Note that in Fig. 11, pattern I (for $N_{Br} = 0$) is quite symmetric, while the outer interface of pattern II (for $N_{Br} = 1$) is evidently asymmetric (it is rotated with respect to the orientation of the inner interface), pattern III (for $N_{Br} = 3$) shows a bit less asymmetric outer interface, and finally pattern IV (for $N_{Br} = 8$) displays a pattern having a fairly more symmetric outer interface. On the other hand, by analyzing Fig. 11 the asymmetry of the inner interfaces is not as evident as those unveiled by the outer borders of the annuli.

It turns out that the asymmetry behaviors of the inner interfaces are a bit different from the ones discussed above for the outer boundaries. This can be verified by examining Fig. 10(b). Contrary to what happens in Fig. 10(a), in Fig. 10(b) one can see that for $N_{Br} \geqslant 1$ the asymmetry tends to decrease as Υ is increased. Another interesting aspect revealed by the data in Fig. 10(b) is that, depending on the

value of Υ, the asymmetry can either increase or decrease as N_{Br} is enlarged. It is also interesting to point out that in both Figs. 10(a) and 10(b) the asymmetry function $As(t)$ can change sign (from negative to positive) as the parameters Υ and N_{Br} are changed. Therefore, from the discussion of Figs. 10 and 11, we conclude that for given values of Υ and N_{Ba}, proper manipulation of the radial magnetic field component (via N_{Br}) can be instrumental to determine the asymmetry properties of the outer and inner boundaries of the MR fluid annular patterns.

IV. CONCLUSION

In this work, we have studied the early nonlinear dynamics of a MR fluid annulus, bordered by a nonmagnetic fluid, in a Hele-Shaw cell. The annular ring structure is under the influence of an in-plane magnetic field which is a combination of a radial and an azimuthal external magnetic field. A perturbative, second-order mode-coupling theory has been employed to study the distinctive interfacial pattern formation resulting from the interaction of hydrodynamic, magnetic, and yield-stress effects.

Our early nonlinear results revealed the development of rotating, stationary state annular shapes presenting fingered protrusions that may arise on the inner, outer, or even on both boundaries of the MR fluid ring. Our theoretical scheme allows one to probe a number of key morphological features and dynamical responses of such annular patterns: in particular, those related to the symmetry properties of the deformed interfaces, and the rotation velocities of the resulting permanent profile shapes. We have found that many of these important features of the ring-shaped patterns can be controlled by tuning the magnitudes of the radial and azimuthal applied magnetic field components (N_{Br} and N_{Ba}), the magnetic yield stress properties of the MR fluid (Υ), and the coupling strength between the internal and external interfaces of the annulus (R). Representative collections of possible MR fluid annular shapes have been provided to highlight these various findings.

The possibility of properly adjusting both the shape and nonlinear dynamical responses of such confined MR fluid annuli may find diverse future applications. As discussed in the introduction of this work, very recent studies have investigated the potential usefulness of both ferrofluid [19–25] and MR fluid [26] simply and doubly connected droplets to serve as magnetically controllable, fluid-based soft robots. These investigations have argued that owing to their unique controllability, deformability, and adaptability, magnetic fluid annular structures could be used in a wide range of applications including organ-on-a-chip, microfluidics, control drug delivery, and enhanced mixing in restricted spaces. We hope that our current theoretical study on magnetic-field-manageable MR fluid annuli in the Hele-Shaw cell apparatus offers an additional tool for exploring and testing some of these practical applications under a well controlled, spatially confined environment.

APPENDIX: SECOND-ORDER MODE-COUPLING FUNCTIONS

In this Appendix we give the expressions for the second-order mode-coupling functions which have been presented in Sec. II.

The second-order functions appearing in Eq. (13) are written as

$$
F(n, p) = -\frac{|n|}{R_1}\Bigg\{ \frac{1}{R_1^3}\Big[1 - \frac{p}{2}(3p + n) \Big]
$$
$$
+ \frac{\chi}{2}\Big[(1 + \chi)N_{Br} + 3\frac{N_{Ba}}{R_1^4}
$$
$$
+ \chi\Big(N_{Br} - \frac{N_{Ba}}{R_1^4} \Big)p(n - p) \Big]
$$
$$
+ \frac{3\Upsilon}{R_1}\Big[\frac{N_{B_a}}{R_1^2} - N_{B_r}R_1^2 \Big]
$$
$$
+ ip\chi^2 \mathrm{sgn}(I)\frac{\sqrt{N_{Ba}N_{Br}}}{R_1^2} \Bigg\}, \tag{A1}
$$

$$
G(n, p) = \frac{1}{R_1}\Bigg\{ |n|[1 - g_1(n, p)\,\mathrm{sgn}(np)] - \frac{1}{f_1} \Bigg\}, \tag{A2}
$$

where

$$
g_1(n, p) = \frac{(1 - R^{2|n|})(1 + R^{2|p|})}{(1 + R^{2|n|})(1 - R^{2|p|})}. \tag{A3}
$$

In addition,

$$
H(n, p) = -\frac{|n|}{R_2}\Bigg\{ \frac{1}{R_2^3}\Big[1 - \frac{p}{2}(3p + n) \Big]
$$
$$
- \frac{\chi}{2}\Big[(1 + \chi)N_{Br} + 3\frac{N_{Ba}}{R_2^4}
$$
$$
+ \chi\Big(N_{Br} - \frac{N_{Ba}}{R_2^4} \Big)p(n - p) \Big]
$$
$$
+ \frac{3\Upsilon}{R_2}\Big[\frac{N_{B_a}}{R_2^2} - N_{B_r}R_2^2 \Big]
$$
$$
- ip\chi^2 \mathrm{sgn}(I)\frac{\sqrt{N_{Ba}N_{Br}}}{R_2^2} \Bigg\}, \tag{A4}
$$

$$
I(n, p) = -\frac{|n|}{R_2}, \tag{A5}
$$

and

$$
J(n, p) = \frac{|n|}{R_1}\Bigg\{ \frac{(-R^{2|n|} + 1)R^{|p|-|n|}}{1 - R^{2|p|}}\mathrm{sgn}(np) \Bigg\}. \tag{A6}
$$

The second-order expressions in Eq. (14) are given by

$$
\mathcal{F}(n, p) = H(n, p), \tag{A7}
$$

$$
\mathcal{G}(n, p) = -\frac{1}{R_2}\Bigg\{ |n|[1 + g_1(n, p)\,\mathrm{sgn}(np)] + \frac{1}{f_1} \Bigg\}, \tag{A8}
$$

$$
\mathcal{H}(n, p) = F(n, p), \tag{A9}
$$

$$
\mathcal{I}(n, p) = \frac{|n|}{R_1}, \tag{A10}
$$

and

$$
\mathcal{J}(n, p) = \frac{|n|}{R_2}\Bigg\{ \frac{(R^{2|n|} - 1)R^{|p|-|n|}}{1 - R^{2|p|}}\mathrm{sgn}(np) \Bigg\}. \tag{A11}
$$

[1] R. E. Rosensweig, *Ferrohydrodynamics* (Cambridge University Press, Cambridge, U.K., 1985).

[2] E. Blums, A. Cebers, and M. M. Maiorov, *Magnetic Fluids* (de Gruyter, New York, 1997).

[3] B. M. Berkovsky and V. Bashtovoy, *Magnetic Fluids and Applications Handbook* (Begell House, New York, 1996).

[4] J. M. Ginder, Behavior of magnetorheological fluids, MRS Bull. **23**, 26 (1998).

[5] G. Bossis, S. Lacis, A. Meunier, and O. Volkova, Magnetorheological fluids, J. Magn. Magn. Mater. **252**, 224 (2002).

[6] S. Genç and P. P. Phulé, Rheological properties of magnetorheological fluids, Smart Mater. Struct. **11**, 140 (2002).

[7] S. A. Lira and J. A. Miranda, Field-controlled adhesion in confined magnetorheological fluids, Phys. Rev. E **80**, 046313 (2009).

[8] R. H. Ewoldt, P. Tourkine, G. H. McKinley, and A. E. Hosoi, Controllable adhesion using field-activated fluids, Phys. Fluids **23**, 073104 (2011).

[9] D. Andelman and R. E. Rosensweig, Modulated phases: Review and recent results, J. Phys. Chem. B **113**, 3785 (2009).

[10] I. Torres-Díaz and C. Rinaldi, Recent progress in ferrofluids research: Novel applications of magnetically controllable and tunable fluids, Soft Matter **10**, 8584 (2014).

[11] X. Zhang, L. Sun, Y. Yu, and Y. Zhao, Flexible ferrofluids: Design and applications, Adv. Mater. **31**, 1903497 (2019).

[12] M. Kole and S. Khandekar, Engineering applications of ferrofluids: A review, J. Magn. Magn. Mater. **537**, 168222 (2021).

[13] K. Ulbrich *et al.*, Targeted drug delivery with polymers and magnetic nanoparticles: Covalent and noncovalent approaches, release control, and clinical studies, Chem. Rev. **116**, 5338 (2016).

[14] G. Huang *et al.*, Magnetically actuated droplet manipulation and its potential biomedical applications, ACS Appl. Mater. Interfaces **9**, 1155 (2017).

[15] V. Socoliuc *et al.*, Ferrofluids and bio-ferrofluids: Looking back and stepping forward, Nanoscale **14**, 4786 (2022).

[16] J. de Vicente, D. J. Klingenbergb, and R. Hidalgo-Alvarez, Magnetorheological fluids: A review, Soft Matter **7**, 3701 (2011).

[17] J. R. Morillas and J. de Vicente, Magnetorheology: A review, Soft Matter **16**, 9614 (2020).

[18] S. Thiagarajan and A. S. Koh, Performance and stability of magnetorheological fluids: A detailed review of the state of the art, Adv. Eng. Mater. **23**, 2001458 (2021).

[19] R. Seemann, M. Brinkmann, T. Pfohl, and S. Herminghaus, Droplet based microfluidics, Rep. Prog. Phys. **75**, 016601 (2012).

[20] Y. Zhang and N.-T. Nguyen, Magnetic digital microfluidics: A review, Lab Chip **17**, 994 (2017).

[21] J. Čejkova, J. Čejková, M. M. Hanczyc, and F. Štěpánek, Droplets as liquid robots, Artif. Life **23**, 528 (2017).

[22] W. Yu *et al.*, A ferrobotic system for automated microfluidic logistics, Sci. Robot. **5**, eaba4411 (2020).

[23] A. Li *et al.*, Programmable droplet manipulation by a magnetic-actuated robot, Sci. Adv. **6**, eaay5808 (2020).

[24] X. Fan, X. Dong, A. C. Karacakol, H. Xie, and M. Sitti, Reconfigurable multifunctional ferrofluid droplet robots, Proc. Natl. Acad. Sci. U.S.A. **117**, 27916 (2020).

[25] V. Nasirimarekani, F. Benito-Lopez, and L. Basabe-Desmonts, Tunable superparamagnetic ring (tSPRing) for droplet manipulation, Adv. Funct. Mater. **31**, 2100178 (2021).

[26] M. Sun *et al.*, Reconfigurable magnetic slime robot: Deformation, adaptability, and multifunction, Adv. Funct. Mater. **32**, 2112508 (2022).

[27] See also news article at https://www.newscientist.com/article/2314395-robot-made-of-magnetic-slime-could-grab-objects-inside-your-body/, and a related video at https://www.newscientist.com/video/2314435-the-magnetic-slime-that-could-retrieve-accidentally-swallowed-objects/.

[28] Q. Pankhurst, N. Thanh, S. Jones, and J. Dobson, Progress in applications of magnetic nanoparticles in biomedicine, J. Phys. D **42**, 224001 (2009).

[29] A. Zakinyan, E. Beketova, and Y. Dikansky, Flows and instabilities of ferrofluids at the microscale, Microfluid Nanofluid. **21**, 88 (2017).

[30] B. Jha, L. Cueto-Felgueroso, and R. Juanes, Fluid Mixing from Viscous Fingering, Phys. Rev. Lett. **106**, 194502 (2011).

[31] P. G. Saffman and G. I. Taylor, The penetration of a fluid into a porous medium or Hele-Shaw cell containing a more viscous liquid, Proc. R. Soc. London A **245**, 312 (1958).

[32] For review articles on Hele-Shaw cell flows, see, for instance, G. M. Homsy, Viscous fingering in porous media, Annu. Rev. Fluid Mech. **19**, 271 (1987); K. V. McCloud and J. V. Maher, Experimental perturbations to Saffman-Taylor flow, Phys. Rep. **260**, 139 (1995); J. Casademunt, Viscous fingering as a paradigm of interfacial pattern formation: Recent results and new challenges, Chaos **14**, 809 (2004).

[33] P. O. S. Livera, P. H. A. Anjos, and J. A. Miranda, Ferrofluid annulus in crossed magnetic fields, Phys. Rev. E **105**, 045106 (2022).

[34] Z. Yu and I. C. Christov, Tuning a magnetic field to generate spinning ferrofluid droplets with controllable speed via nonlinear periodic interfacial waves, Phys. Rev. E **103**, 013103 (2021).

[35] J. A. Miranda, Rotating Hele-Shaw cells with ferrofluids, Phys. Rev. E **62**, 2985 (2000).

[36] T. John, K. May, and R. Stannarius, Meniscus of a ferrofluid around a vertical cylindrical wire carrying electric current, Phys. Rev. E **83**, 056308 (2011).

[37] R. M. Oliveira, J. A. Miranda, and E. S. G. Leandro, Ferrofluid patterns in a radial magnetic field: Linear stability, nonlinear dynamics, and exact solutions, Phys. Rev. E **77**, 016304 (2008).

[38] C.-Y. Chen, W.-L. Wu, and J. A. Miranda, Magnetically induced spreading and pattern selection in thin ferrofluid drops, Phys. Rev. E **82**, 056321 (2010).

[39] R. M. Oliveira, I. M. Coutinho, P. H. A. Anjos, and J. A. Miranda, Shape instabilities in confined ferrofluids under crossed magnetic fields, Phys. Rev. E **104**, 065113 (2021).

[40] R. B. Bird, R. Armstrong, and O. Hassager, *Dynamics of Polymeric Liquids* (Wiley, New York, 1977).

[41] G. H. Covey and B. R. Stanmore, Use of the parallel-plate plastometer for the characterisation of viscous fluids with a yield stress, J. Non-Newtonian Fluid Mech. **8**, 249 (1981).

[42] A. Cebers and M. M. Maiorov, Magnetostatic instabilities in plane layers of magnetizable liquids, Magnetohydrodynamics (NY) **16**, 21 (1980).

[43] A. Cebers, Dynamics of magnetostatic instabilities, Magnetohydrodynamics (NY) **17**, 113 (1981).

[44] D. P. Jackson, R. E. Goldstein, and A. O. Cebers, Hydrodynamics of fingering instabilities in dipolar fluids, Phys. Rev. E **50**, 298 (1994).

[45] J. V. Fontana, S. A. Lira, and J. A. Miranda, Radial viscous fingering in yield stress fluids: Onset of pattern formation, Phys. Rev. E **87**, 013016 (2013).

[46] P. Coussot, Saffman-Taylor instability in yield-stress fluids, J. Fluid Mech. **380**, 363 (1999).

[47] M. Igonin, Hydrodynamic instabilities of miscible and immiscible magnetic fluids in a Hele-Shaw cell, Ph.D. thesis, D. Diderot University Paris 7, 2004.

[48] J. A. Miranda and M. Widom, Radial fingering in a Hele-Shaw cell: A weakly nonlinear analysis, Physica D **120**, 315 (1998).

[49] P. H. A. Anjos and S. Li, Weakly nonlinear analysis of the Saffman-Taylor problem in a radially spreading fluid annulus, Phys. Rev. Fluids **5**, 054002 (2020).

[50] E. O. Dias, S. A. Lira, and J. A. Miranda, Interfacial patterns in magnetorheological fluids: Azimuthal field-induced structures, Phys. Rev. E **92**, 023003 (2015).

[51] P. H. A. Anjos, S. A. Lira, and J. A. Miranda, Fingering patterns in magnetic fluids: Perturbative solutions and the stability of exact stationary shapes, Phys. Rev. Fluids **3**, 044002 (2018).

[52] S. A. Lira, J. A. Miranda, and R. M. Oliveira, Field-induced patterns in confined magnetorheological fluids, Phys. Rev. E **81**, 046303 (2010).

[53] L. N. Brush and R. F. Sekerka, A numerical study of two-dimensional crystal growth forms in the presence of anisotropic growth kinetics, J. Cryst. Growth **96**, 419 (1989).

[54] L. N. Brush, R. F. Sekerka, and G. B. McFadden, A numerical and analytical study of nonlinear bifurcations associated with the morphological stability of two-dimensional single crystals, J. Cryst. Growth **100**, 89 (1990).

[55] S. W. Haan, Weakly nonlinear hydrodynamic instabilities in inertial fusion, Phys. Fluids B: Plasma Phys. **3**, 2349 (1991).

[56] H. Guo, D. C. Hong, and D. A. Kurtze, Surface-Tension-Driven Nonlinear Instability in Viscous Fingers, Phys. Rev. Lett. **69**, 1520 (1992).

[57] H. Guo, D. C. Hong, and D. A. Kurtze, Dynamics of viscous fingers and threshold instability, Phys. Rev. E **51**, 4469 (1995).

[58] E. Alvarez-Lacalle, J. Casademunt, and J. Ortín, Systematic weakly nonlinear analysis of interfacial instabilities in Hele-Shaw flows, Phys. Rev. E **64**, 016302 (2001).

[59] E. Alvarez-Lacalle, E. Pauné, J. Casademunt, and J. Ortín, Systematic weakly nonlinear analysis of radial viscous fingering, Phys. Rev. E **68**, 026308 (2003).

[60] P. P. Phulé and J. M. Ginder, Synthesis and properties of novel magnetorheological fluids having improved stability and redispersibility, Int. J. Mod. Phys. B **13**, 2019 (1999).

[61] P. Kuzhir, M. T. López-López, and G. Bossis, Abrupt contraction flow of magnetorheological fluids, Phys. Fluids **21**, 053101 (2009).

[62] See Supplemental Material at http://link.aps.org/supplemental/10.1103/PhysRevE.106.025105 for videos illustrating the rotation process of the MR fluid annular patterns shown in Figs. 2 and 7.

[63] A. B. Kennedy, Q. Chen, J. T. Kirby, and R. A. Dalrymple, Boussinesq modeling of wave transformation, breaking, and runup. I: 1D, J. Waterw. Port. Coast. **126**, 39 (2000).

[64] T. J. Maccarone, The biphase explained: Understanding the asymmetries in coupled Fourier components of astronomical time series, Mon. Not. R. Astron. Soc. **435**, 3547 (2013).